Extension modes and breakup processes of the Southeast China-Northwest Palawan conjugate rifted margins

Nirrengarten M.[1], Mohn G.[1], Kusznir N.J.[2], Sapin F.[3], Despinois F.[3], Pubellier M.[4], Chang S.P.[4], Larsen H.C.[5,6], Ringenbach J.C.[3]*

[1] *Département Géosciences et Environnement, Université de Cergy-Pontoise, Cergy-Pontoise, France*
[2] *Department of Earth and Ocean Sciences, University of Liverpool, Liverpool, UK*
[3] *Total SA, CSTJF, Pau, France*
[4] *Laboratoire de Géologie, UMR 8538, École Normale Supérieure, CNRS, Paris, France*
[5] *State Key Laboratory of Marine Geology, Tongji University, Shanghai, China.*
[6] *Geological Survey of Denmark and Greenland, Copenhagen, Denmark*

***Corresponding author:**
Michael Nirrengarten
michael.nirrengarten@u-cergy.fr
Laboratoire GEC, Université de Cergy Pontoise
1 rue Descartes
95000 Neuville-sur-Oise, France

Keywords: Conjugate rifted margins; South China Sea breakup; IODP Expedition 367-368; Gravity modelling

Abstract:

Our understanding of continent-ocean transition structures and magmatism in the absence of excessive magmatic additions has been guided by the observations and models developed at the magma-poor Iberia-Newfoundland conjugate margins. Recently these models have been challenged in the South China Sea in light of new IODP Expeditions 367-368-368X. We have used an integrated analysis of high quality seismic reflection and gravity anomaly data, calibrated against recent deep sea drilling results, to investigate margin structure and tectono-magmatic interplay during continental breakup and early seafloor spreading between the SE China-NW Palawan conjugate margins.

The Eocene-Oligocene South China Sea rifting initiates in a heterogeneous and likely thermally un-equilibrated lithosphere formed by the Mesozoic Yenshanian orogeny. Gravity and joint inversion methods confirm lateral variation of basement densities across the conjugate margins. Lithospheric and basement heterogeneities induced a rifting style characterized by a series of highly thinned rift basins associated with extensional faulting soling out at various crustal levels. Final rifting in late Eocene triggered decompression melting forming mid-ocean ridge type magmatism, which emplaced within thinned continental crust as deep intrusions and shallow extrusive rocks. This initial magmatic activity was concomitant with continued deformation of continental crust by extensional faulting. Integrated analysis of seismic reflection profiles and gravity anomaly data combined with deep-sea boreholes accurately locate the continent-ocean boundary. We show that the initial igneous crust, continentward of oceanic magnetic anomaly C10n, is asymmetric in width and in morphology for the conjugate margins. The wider and faulted newly accreted domain on the SE China side indicates that magmatic accretion is associated with tectonic faulting during the formation of initial oceanic lithosphere. We suggest that deformation was not symmetrically distributed between the conjugate margins during the initiation of seafloor spreading but evolved asymmetrically until the stabilisation of the spreading ocean ridge around C10n. The analysis of the South China Sea breakup reveals a transient interplay between faulting, magmatic budget and extension rates during the formation of the continent-ocean transition and initial emplacement of igneous crust.

1. Introduction

Rifting processes may result in continental breakup through the extension and thinning of continental lithosphere. Continental breakup mechanisms are recorded within the Continent-Ocean Transition (COT) of passive margins where continental extension evolves into localized accretion of new oceanic lithosphere (Dewey and Bird, 1970; Falvey, 1974; Heezen, 1960; McKenzie, 1978; Whitmarsh et al., 2001). Such mechanisms are by definition transient and characterized by complex tectono-magmatic interplays evolving through time and operating on inherited heterogeneous lithosphere (e.g. Petri et al., 2019; Reston, 2009; Taylor et al., 1999). Seismic images of rifted margins show large variability of COT architectures indicating different tectono-magmatic processes. Extensional structures interpreted in the COT such as high angle normal or low angle extensional faults depend on the rheological inheritance and evolution of the crust and underlying mantle during rifting (e.g. crustal embrittlement (Pérez-Gussinyé et al., 2003), and lower crustal ductility (Brune et al., 2017; Clerc et al., 2018, 2015; Huismans and Beaumont, 2011). In general, extension and lithospheric thinning trigger decompression melting and Mid-Ocean Ridge Basalt (MORB) type magmatism at COTs (Mckenzie and Bickle, 1988). Timing, volume and localization of this magmatism are highly variable in the COT and are controlled among others by extension rate, initial lithosphere geotherm, crustal rheology, initial crustal thickness and inheritance (Davis and Lavier, 2017). In that context, when analysing the development of rifted margins from rift initiation to the stable accretion of an oceanic lithosphere, it is fundamental to address the timing and relative importance of tectonic and magmatic processes, including symmetric or asymmetric evolution of paired conjugate margins. As already identified in the 80s by the IPOD (International Phase of Ocean Drilling) program on passive continental margins (Curray, 1980), without drilling data, the interplay in time and space between crustal deformation, lithospheric thinning and magmatism remains unresolved.

In that perspective, the South China Sea (SCS) rifted margins represent a key natural laboratory benefiting from extensive long offset seismic reflection and refraction profiles (e.g. Gao et al., 2015; Pichot et al., 2014; Pin et al., 2001; Yang et al., 2018; Lei and Ren, 2016) in combination with borehole data (Larsen et al., 2018e; Li et al., 2015) from both academic and industrial surveys. The rifted continental domain leading to the formation of the SCS oceanic domain is remarkably wide (>600 km cumulated over both conjugate margins), but is not equally distributed between the SE China and the NW Palawan conjugate margins (Fig. 1). Results from the recent IODP (International Ocean Discovery Program) Expeditions 367-368-368X, with six boreholes drilling the acoustic basement on the ~400 km wide SE China (Larsen et al., 2018d), revealed the presence in its distal parts of a sharp transition from thinned continental crust to igneous crust. This contrasts markedly with the only other extensively drilled COT, the North Atlantic magma-poor Iberia-Newfoundland margins, where large domains (>100 km) of exhumed continental lithospheric mantle have been sampled by drilling on both conjugate margins (Boillot et al., 1987; Tucholke and Sibuet, 2007; Whitmarsh et al., 1996; Whitmarsh and Wallace, 2001). The evolution of the SE China margin COT and initial seafloor spreading, however, have not been yet fully integrated with that of its conjugate NW Palawan margin.

Therefore, this contribution, combining available geological and geophysical datasets, aims to analyse the nature and architecture of the SE China-NW Palawan conjugate margins to assess the interactions between extension, faulting and magmatic additions during breakup and early stages of oceanic accretion. We use reflection seismic lines on both the distal SE China and NW Palawan margins combined with 3D free-air gravity anomaly inversion to determine their crustal architectures. In addition, we have performed joint inversion of seismic reflection and gravity anomaly data. This allows us to determine crustal thickness and crustal density variations reflecting structural and crustal domain boundaries on a regional scale. The IODP drilling results offer critical local constraints on basement nature and on the timing of rifting and breakup. The SE China-NW Palawan conjugate margins presents a scenario of late rifting and breakup evolution that differs from other drilled conjugate systems (Iberia-Newfoundland (Mohn et al., 2015; Tucholke et al., 2007)

2. Geological setting

2.1) South China Sea tectonic evolution

The SCS is a south-westward oriented V-shaped oceanic basin (~1200 km long and a maximum width of ~800km) of Oligocene to mid Miocene age (Fig. 1, Briais et al., 1993; Taylor and Hayes, 1983). The eastern part of SCS oceanic lithosphere is currently subducting beneath the Manilla Trench to the East. Initiation of this subduction zone started likely in early Miocene (Arfai et al., 2011; de Boer et al., 1980) contemporaneously with the cessation of the SCS spreading (Franke et al., 2014) and with large left-lateral movement of the Philippines Islands toward the north. This motion is interpreted as related to the northward drift of the Australia plate that strongly deformed the eastern border of the Sunda Plate during the Neogene (Pubellier et al., 2003). Variable ages for seafloor spreading cessation were proposed based on oceanic magnetic anomaly modelling (20.5 Ma (Barckhausen et al., 2014), 15.5 Ma (Briais et al., 1993) or 15 Ma (C.-F. Li et al., 2014)). The SCS oceanic domain can be divided into three well defined segments (Eastern, Northwestern and Southwestern sub-basins) (Fig. 1) reflecting spreading axis jumps and changes in spreading ridge orientation (Briais et al., 1993; Sibuet et al., 2016) as well as a propagation of breakup toward the southwest.

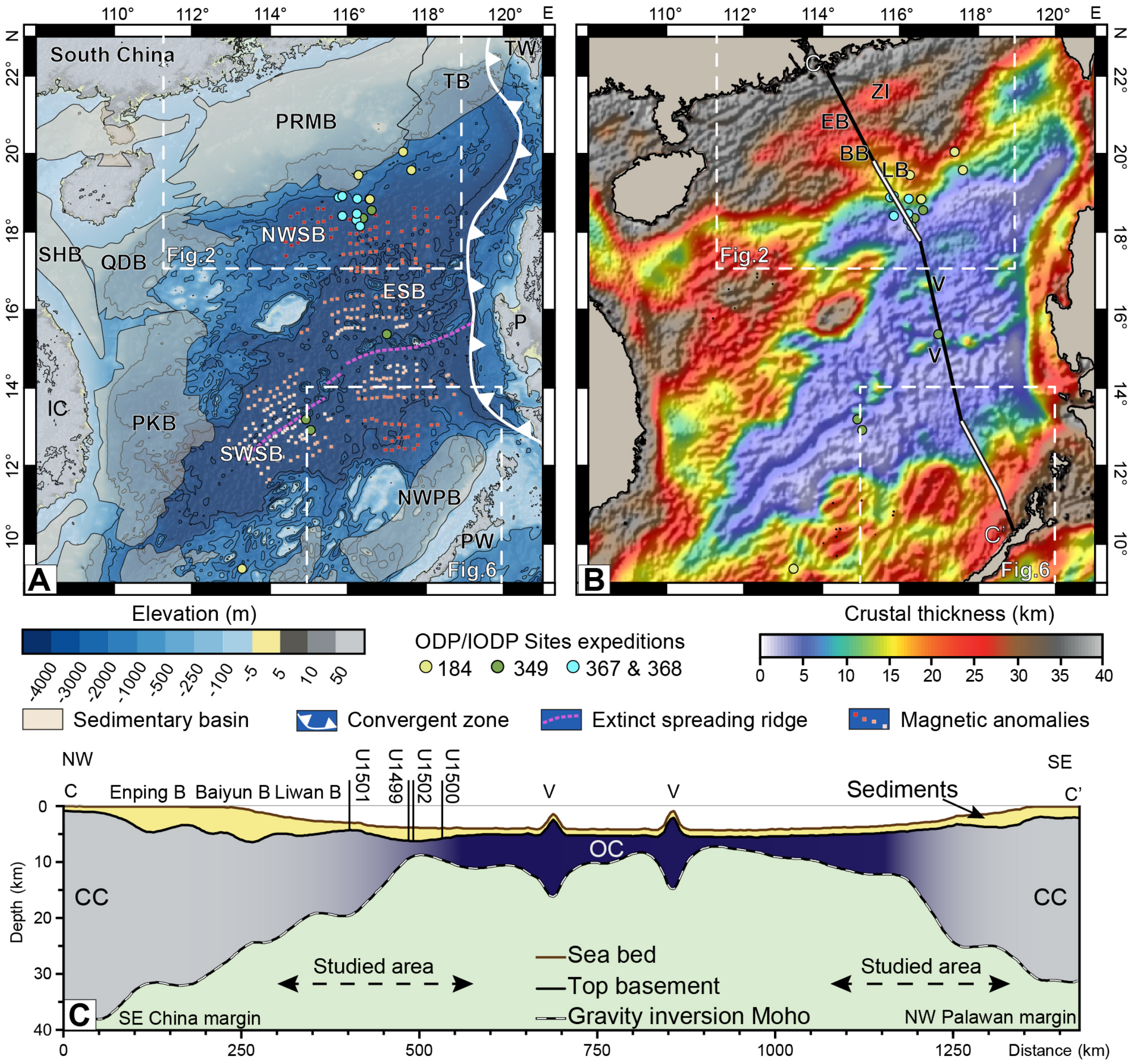

Figure 1: A) Topographic map of the SCS (Amante & Eakins, 2009) associated with the oceanic magnetic anomalies (Briais et al., 1993) B) Crustal thickness map determined by 3D gravity

anomaly inversion with the free-air gravity anomaly in shaded relief (Gozzard et al., 2019) and the location of profile C C) Profile extracted from the crustal thickness map determined by 3D gravity anomaly inversion (Gozzard et al., 2019) crossing the SCS from SE China to NW Palawan coast. BB: Baiyun Basin, CC: Continental Crust EP: Enping Sub-Basin, ESB: East sub-basin IC: Indochina, QB: Qiongdongnan Basin, LB: Liwan Sub-Basin, NWPB: Northwest Palawan Basin, NWSB: Northwestern Sub-Basin, OC: Oceanic crust, P: Philippines, PKB: Phu Khan Basin, PRMB: Pearl River Mouth Basin, PW: Palawan, SHB: Song Hong-Yinggehai Basin, SWSB: Southwest Sub-Basin, TB: Tainan Basin, TW: Taiwan, V: Volcano, ZI: Zhu I Basin

The oldest oceanic crust has been dated by magnetic modelling at 33-32 Ma in the Eastern oceanic sub-basin (Briais et al., 1993; Taylor and Hayes, 1983). The initial N-S direction of SCS spreading continued up to the C6b anomaly (~23 Ma) and is limited to the Eastern and Northwestern sub-basins. Afterward, spreading migrated from NE to SW between ~23 and ~16 Ma and formed the Southwestern sub-basin (Briais et al., 1993; Zhou et al., 1995). This propagation of deformation caused each margin segment to have its own major rifting event and breakup history (Franke et al., 2014; Savva et al., 2014). The variations in the propagation velocity and orientation have been recently interpreted as resulting from out of plane compression forces (Le Pourhiet et al., 2018), that might be caused by continental lithosphere masses reorganisation during Himalayan growth and kinematic reorganisation.

Rifting of the SCS continental lithosphere occurred in a very wide domain (>600 km) characterised by several thick sedimentary basins (e.g. Pearl River Mouth (PRMB), Phuh Khan, Tainan) (Hayes and Nissen, 2005; Ru and Pigott, 1986) (Figs. 1, 2). The age of initial rifting in the SCS is not fully resolved. Most of the industry boreholes across the sedimentary basins on the proximal margin are located on basement highs and record condensed continental facies, whose dates from palynology are only poorly resolved. In the Eastern sub-basin, ages of rifting are mainly based on the evolution of the PRMB. This basin shows evidence for two phases of extension preceding continental breakup, one of Late Cretaceous to early Paleocene age and a second of middle Eocene to early Oligocene age (Ru and Pigott, 1986; Zhou et al., 1995). The first Late Cretaceous to early Paleocene rift event is associated with the deposition of the Shenhu Formation characterized by continental clastic sedimentation containing many metamorphic and volcanic fragments (Sizhong and Cunmin, 1993; Zhou et al., 1995) (Fig. 3). This event is associated to the post-orogenic dismantling of the Yenshanian Arc (Klimetz, 1983).

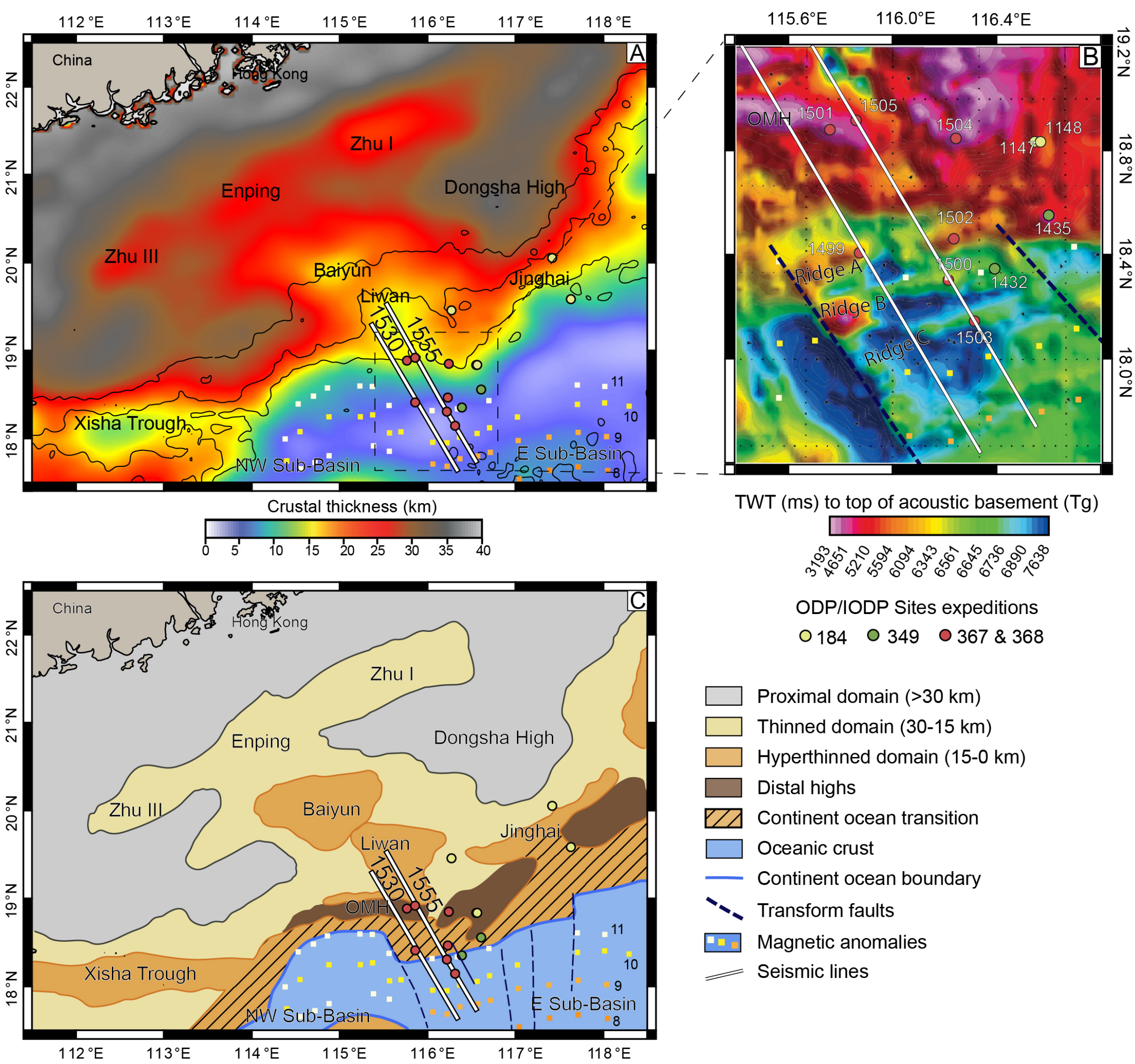

Figure 2: A) Crustal thickness map of the SE China margin determined by 3D gravity inversion B) Zoomed map of the Tg reflector (i.e. top acoustic basement, see text) on the margin segment cored during IODP Expeditions 367 & 368 (Larsen et al., 2019d), C) Rift domain map of the SE China margin. Picking of the oceanic magnetic anomalies from Briais et al., 1993

The later middle Eocene to early Oligocene rift event was associated in the PRMB with the deposition of the Wenchang lacustrine and the Enping lacustrine to shallow marine formations (Sizhong and Cunmin, 1993) (Fig. 3). These sedimentary sequences are contemporaneous with the formation of deep sedimentary basins (e.g. Baiyun, Liwan sub-basins, Fig. 2) bounded by low angle extensional faults soling out at mid crustal levels (Savva et al., 2014; Lei et al., 2019). This second event is interpreted to represent the main rifting phase that thinned the continental crust (beta factor>3) (Haizhang et al., 2017; Larsen et al., 2018d)

Recent IODP scientific boreholes on the hitherto un-sampled distal margin recovered pre- syn- and post-rift sediments (Fig. 3) (Larsen et al., 2018d). The sedimentary facies and horizon ages of seismic interpretations, now firmly constrain continental breakup in the Eastern SCS sub-basin to be in the Early Oligocene (~30 Ma) (Larsen et al., 2018d). However, southwest of the PRMB, the continental extension continues into the lower Miocene and the opening of the southwestern segment of the SCS.

Several authors (Holloway, 1981; Li and Li, 2007; Pubellier and Meresse, 2013; Taylor and Hayes, 1983; Ye et al., 2018) proposed that during the Mesozoic, the northern margin of the SCS was an “Andean” type active margin with compressional structures and important arc magmatism related to the northward subduction of the proto-Pacific Ocean below the SE China block. The last occurrence of subduction related magmatism is dated at 86 Ma (J. Li et al., 2014), implying that no more than 50 Myrs separated convergence from initiation of SCS rifting. This is less than the estimated time required for lithosphere to regain thermal equilibrium (McKenzie, 1978).

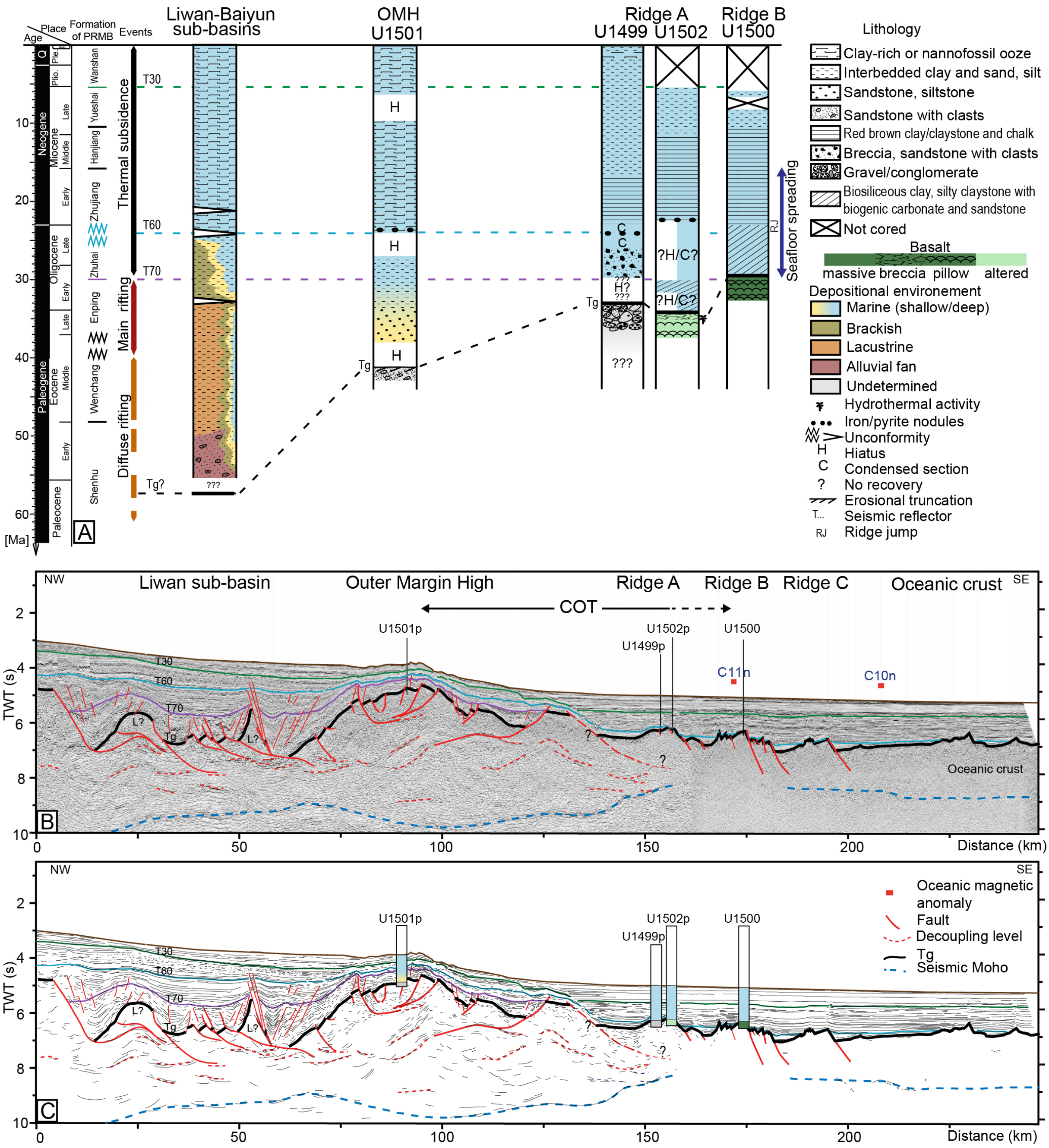

Figure 3: A) Summary charts of drilling results from IODP 367-368 (Larsen et al., 2018e). Synthetic stratigraphic columns of Liwan/Baiyun sub-basins (Morley, 2016). B) Seismic section 1555 interpreted with the major horizons and unconformities (modified from Larsen et al., 2018d). Location of seismic section 1555 is presented in Figure 2. L indicates potential emplacement of laccolith; Tg, top of acoustic basement. C) Line Drawing of the seismic section 1555

2.2) The conjugate SE China-NW Palawan distal margins structure

Plate kinematic reconstructions of Taylor and Hayes (1983) and Zahirovic et al., (2014) identify the NW Palawan margin as the conjugate margin segment of the IODP studied segment of the SE China margin within the western part of the Eastern sub-basin (Fig. 1). We have selected representative seismic sections from each side of these two conjugate margins segments to compare their development.

2.2.1) The SE China distal margin

The SE China margin facing the Eastern SCS oceanic sub-basin is a wide margin (> 400 km) (Fig. 2). The PRMB occupies most of this margin with numerous deep rift basins (e.g. Baiyun, Enping, Liwan sub-basins Fig. 2) separated by basement highs (e.g. Outer Marginal High, Fig.2) which have been extensively investigated by seismic reflection data and industry drilling (Gao et al., 2015; Lei et al., 2019; Lei and Ren, 2016; Zhou et al., 2018; Lei et al., 2018). The PRMB developed during the Eocene to early Oligocene main rifting phase and was later progressively filled by thick post-rift sedimentary sequences. Parts of the deeper structures of the PRMB were likely inherited from the Mesozoic convergent setting as expressed by remnants of thrust and folds in the substratum (Li et al., 2008; Ye et al., 2018). Hydrocarbon exploration focuses on the proximal part of the margin (Ge et al., 2017), but the more distal domain hosting the COT is nevertheless covered by high quality seismic reflection (Ding et al., 2018; Gao et al., 2015), seismic refraction profiles (Lester et al., 2014; Pin et al., 2001; Zhao et al., 2010) and potential field surveys (C.-F. Li et al., 2014). These data constrained breakup models highlighting the lateral propagation of oceanic accretion (Cameselle et al., 2017; Lei and Ren, 2016). In this study, we focus on a ~100km long segment of the distal SE China margin (Fig. 2) where synchronous breakup and similar deformation processes can be assumed. This margin segment is covered by high quality seismic data (Fig. 4-5) and located at the western edge of the Eastern oceanic sub-basin where seven deep scientific drill holes, including six reaching the acoustic basement have been cored during IODP Expeditions 367-368 and 368X (Larsen et al., 2018d, Childress et al., 2019) (Fig. 2). This segment is characterized by a major basement high referred to as the Outer Marginal High (OMH) separating to the northeast the Liwan sub-basin, and to the southwest the COT (Fig.3). Since the Oligocene breakup, no major tectonic event occurred within this margin segment, while the subduction zone is located 500 km east of the investigated margin segment.

2.2.2) The NW Palawan distal margin

The structure and rifting history of the NW Palawan margin are not constrained with dense modern geophysical surveys and deep scientific boreholes, unlike the SE China margin. However, available seismic profiles and industry wells (mostly from the proximal margin) provide general constraints on the sedimentary evolution and margin architecture (Franke et al., 2011; Schlüter et al., 1996; Steuer et al., 2013; Williams, 1997). A first order observation is that the NW Palawan margin is much narrower (~180 km wide, Fig. 6) compared to the SE China conjugate margin.

North Palawan is interpreted as formerly belonging to the South China block during the Mesozoic and early Cenozoic and shows a similar tectono-stratigraphic evolution to the Asian mainland (Fontaine, 1979; Holloway, 1981). The syn-rift sedimentary sequence of late Eocene to Oligocene age is composed of fluvial to middle neritic interbeded siltstones and sandstones in the proximal domains. In the distal domains, a few drill holes contain continental to outer neritic facies and locally carbonate platforms on basement highs (Franke et al., 2011; Schlüter et al., 1996; Williams, 1997). During rifting in the Eocene to early Oligocene period, the NW Palawan block was also affected by the obduction of the ophiolitic belt outcropping onshore (Faure et al., 1989). A tectonic quiescence followed this synchronous extensional/compressional event with emplacement of the Nido carbonates, at least on the proximal margin, that constitute the latest Eocene to early Miocene late syn- to post-rift sediments (Fig. 7)(Fournier et al., 2005). Since the middle Miocene, the NW Palawan block was affected by the ongoing collision between continental fragments (NW Palawan, the Calamian Group, Mindoro), the magmatic arc and ophiolite units of Luzon in the east (Karig, 1983), but none of this deformation affected the studied distal margin.

3. Data and method

3.1) Dataset and mapping methodology

The SE China margin is covered by a dense grid of geophysical data from which we use two previously published reflection seismic profiles (lines 1555 and 1530 Figs. 4-5, acquisition parameters can be found in Gao et al., 2015). These profiles are located near to IODP drilling Sites (Figs. 2, 3, 4 and 5). For the NW Palawan margin, we use the reflection seismic profile (BGR08-109 Fig. 6, 7) published by Franke et al. (2011). In addition, we include in our analysis of the area: 1) a range of published seismic dataset acquired by both academic and industrial surveys (Cameselle et al., 2017; Lei et al., 2019; Yang et al., 2018) ; 2) a compilation of structural maps (Cullen et al., 2010; Pubellier et al., 2017) ; 3) different borehole data (Larsen et al., 2018e; Li et al., 2015; Wang et al., 2000); 4) magnetic and gravity grids (Doo et al., 2015; Meyer et al., 2017; Sandwell et al., 2014) ; 5) refraction lines (Ding et al., 2012; Pichot et al., 2014; Pin et al., 2001); and 6) crustal thickness mapping determined by gravity inversion (Gozzard et al., 2019).

We follow the rift domain mapping methodology applied for hyper-extended magma-poor margins located around the southern North Atlantic (Nirrengarten et al., 2018; Peron-Pinvidic et al., 2013) on the SE China-NW Palawan conjugate margins (Fig. 2,6). This method is based on the identification of characteristic elements of each rift domains such as crustal thickness, structural style, accommodation space and geometry of the sedimentary infill (for a detailed description see Tugend et al., 2015). Several domains were defined alongside both margins such as: proximal, thinned and hyper-thinned domains, distal highs, COT, oceanic crust (Fig. 2-6). In this study, the proximal domain is defined by a crustal thickness exceeding 30 km on the gravity inversion crustal thickness map (Fig.2). In seismic sections this domain is characterized by small rift basins bounded by high angle normal faults. The thinned and hyper-thinned domains correspond to continental crust moderately (~30 -15 km thick) to highly thinned (<15 km thick), respectively. Distal highs are present along the SCS margins and correspond to positive basement topography with some of them showing a bathymetric expression today. These distal highs generally delimit thinned or hyper-thinned domains from those of the COT. The COT is located from the distal high to the first igneous oceanic crust. It is composed of the most distal hyper-thinned continental crust overprinted by magmatic additions (Larsen et al., 2018d). The oceanic crust is defined by fully new igneous crust with a crustal thickness ranging from 5 to 7 km (~2s Two Way Travel Time: TWT). Hence the COB (Continent-Ocean Boundary) is the continentward limit of the oceanic crust.

3.2) Quantitative analysis methodology: 3D gravity anomaly inversion and joint inversion of seismic reflection and gravity data

In order to determine Moho depth and crustal basement thickness on the SCS rifted margins we perform 3D spectral domain gravity inversion following the scheme of Parker (1972) together with a correction for the lithosphere thermal gravity anomaly and a parameterization of decompression melting to predict magmatic addition (Chappell and

Kusznir, 2008, Alvey et al. 2008, Kusznir et al. 2018). Only public domain data are used for the 3D mapping procedure: free-air gravity anomaly data (1 arc-minute resolution; Sandwell et al., 2014; see supplementary material 1), bathymetry ETOPO1 (1 arc-minute resolution; Amante and Eakins, 2009), NOAA sediment thickness (5 arc-minutes resolution; Whittaker et al., 2013) and oceanic crust age (6 arc-minute resolution; Müller et al., 2016). Prior to the 3D spectral inversion to determine Moho depth, a Butterworth low-cut filter with cut-off wavelength 100 km is applied to the Moho residual gravity anomaly to remove short wavelengths. This gravity inversion scheme invokes Smith's theorem (Smith, 1961) which for the assumptions made provides a unique solution for 3D Moho depth and crustal basement thickness (Chappell & Kusznir 2008)

We follow the parameterization of Gozzard et al., (2019), who performed extensive sensitivity tests on the free-air gravity anomaly inversion for the SCS to determine crustal basement thickness and continental lithosphere thinning. Our preferred solution uses a reference Moho depth at 40 km, normal volcanic addition (giving a 7 km thick oceanic crust) and a breakup age at 33 Ma corresponding to the oldest oceanic crust in the SCS. Gravity inversion using these parameters predicts the seismically observed thicknesses of oceanic crust in the study area. The sensitivity tests carried out by Gozzard et al., 2019 demonstrated the critical importance of including the lithosphere thermal gravity anomaly correction in the gravity inversion.

The 3D gravity anomaly inversion map is improved by the integration of more precise sediment thickness data of seismic lines 1555, 1530 and BGR08-109 (Fig. 4, 5 &7) (Franke et al., 2011; Gao et al., 2015; see supplementary material 2). Sediment thickness is based on a time to depth conversion using depth-time functions established at Sites U1500 and U1499 for the COT and oceanic domain of lines 1555 and 1530 (Stock et al., 2018; Sun et al., 2018). However application of this depth conversion produces unrealistically large interval seismic velocities for sediments in the deeper parts of the Liwan sub-basin as Tg is approached. As a consequence for the Liwan sub-basin (NW of the OMH) and the Palawan section, in the absence of seismic velocity–depth measurements from well data, we use a seismic velocity-depth relationship of $V_p = V_o + k.z$ for depth conversion where $V_o = 1.75$ km.s^{-1}, k = 0.4 km.s^{-1}.km^{-1} and z is in km. This avoids very large and unrealistic interval velocities in the deepest parts of the Liwan sub-basin. It should be noted that this uncertainty in the Liwan sub-basin does not adversely affect our gravity inversion analysis in the COT.

To determine the lateral variation of crustal basement density across the COT margin we perform a joint inversion of the deep seismic reflection interpretation and gravity anomaly data for lines 1555, 1530 and BGR08-109 (Fig. 4, 5 & 7) following the method described in Cowie et al. (2017) and Harkin et al. (2019). This method compares Moho depth determined from gravity inversion with the interpreted seismic Moho TWT in the time domain. By matching the gravity Moho taken into the time domain with the Moho TWT from seismic interpretation, the lateral variation in vertically averaged basement density and seismic velocity can be determined. The conversion of Moho depth to TWT in the time domain requires a value for basement seismic velocity which we determine using an equation linking basement seismic velocity with basement density. In this study we use a linear empirical relationship ($V_p = 2.27.\rho + 0.25$) linking seismic velocity ($V_{p,}$ in km/s) and density (ρ, in gm/cc) for crustal basement determined from the velocity-density compilation presented by Birch (1961) for crystalline crustal basement rocks. An alternative velocity-density relationship based on the Nafe-Drake relationship (Ludwig et al., 1970; Brocher, 2005) has also been examined, however the relationship derived from Birch (1961) gives a more stable joint-inversion and is also more appropriate for crystalline crustal basement. In the initial gravity inversion (prior to the joint inversion iterations), a uniform basement density of 2.85 $g.cm^{-3}$ used.

The lateral variation of basement density affects the depth of the Moho predicted from gravity inversion, while the lateral variation of basement seismic velocity affects the conversion of the gravity inversion Moho from the depth to the time domain. The joint inversion requires an iterative adjustment of both basement density and seismic velocity, which are linked by the velocity-density relationship described above, until convergence is achieved. The advantage of comparing the gravity Moho depth with the seismic Moho in the time domain rather than the depth domain is that this approach avoids the uncertainties in basement seismic velocity which are used in making the seismic reflection depth section. It also provides a powerful technique for validating Moho seismic interpretations.

The method assumes that the sediment thickness (depth to top basement), used in the gravity inversion and derived from the seismic reflection interpretation and depth conversion, is correct. The gravity inversion Moho depth (and seismically determined depth to top basement) is used to determine crustal basement thickness which is converted into the time domain (as an interval TWT). This interval TWT is then added to the seismic interpretation of top basement in TWT to determine the conversion of the gravity inversion Moho in depth into the time domain for direct comparison with the seismic Moho TWT.

The lateral density variations of crustal basement along a transect are used to identify lateral variation in the nature of the crust. This joint inversion is pertinent only when the Moho reflector is well imaged on the seismic sections. The joint inversion analysis was performed across the entire SE China margin and adjacent oceanic crust for seismic lines 1555 and 1530, but only on the oceanic and COT domains of the NW Palawan margin for seismic line BGR08-109 (Fig. 4, 5 &7)

4. Architecture of the SE China margin

4.1) Mapping of the rift domains

Our map of rift domains of the SE China margin shows an alternation of deep rift basins separated by basement highs (Fig. 2). The Zhu I-III and Enping sub-basins are aligned and elongated along a NE-SW axis (Fig. 2). These basins are characterized by moderate crustal thinning (~20 km thick) and constitute the “thinned domain” (Fig. 2A-C). Further seaward, the Baiyun and Liwan sub-basins occupy a central position in the margin representing the “hyper-thinned domain”. Several studies (Lei et al., 2019; Wang et al., 2018; Zhou et al., 2018) show that these basins are floored by hyper-thinned crust (<15 km thick) in relation with low angle extensional faults rooting at mid-crustal level. The Baiyun sub-basin is separated from the Enping sub-basin to the NW and the Liwan sub-basin to the SE by two basement highs with thicker continental crust (~20km). The Liwan sub-basin is separated from the COT by the OMH. This distal high (OMH) shows a significantly shallower Tg (base Cenozoic, see below) on the basement reflector TWT depth map (Fig. 2B). The COT bounding the oceanic domain is 50 to 80 km wide. The mapped COB is segmented by fracture zones. In our focus area (Fig. 2B) a sharp transfer zone is observed to the SW and a more diffuse system to the NE delimiting a ˜150km wide margin segment.

4.2) Seismic architecture and correlation with IODP data

The deep seismic profiles 1555 and 1530 image the distal part of the SE China margin close to the location of the IODP Sites from Expeditions 349, 367, 368 and 368X (Figs. 3-5). Across these two profiles a strong reflector (Tg) can be consistently identified. Tg is the top of acoustic basement, which corresponds locally to the base of the Cenozoic sequence (Fig. 3). The mapping in TWT of Tg reflector across the studied segment of the distal SE China Sea margin (Larsen et al., 2018e) highlights the 3D architecture of this area (Fig. 2B). From northwest to southeast, the following distinct structural features have been recognized (Figs. 3, 4-5): 1) The Liwan sub-basin; 2) The OMH; 3) The COT; 4) Ridges A, B, C; and 5) The oceanic crust (Larsen et al., 2018e). Besides the Tg reflector, key seismic horizons have been determined by correlation between stratigraphic well data and interpreted seismic sections (e.g. Larsen et al., 2018d; Lei et al., 2019). The following seismic horizons used in this study are: T70 corresponding to the top of syn-rift sequence, T60 representing a regional unconformity around Oligocene-Miocene boundary (28-24 Ma) and T30 correlating with the top of the Miocene (Fig. 3).

Seismic lines 1555 and 1530 have been previously described in several previous contributions (Gao et al., 2015, Larsen et al., 2018d). In this section, these works are summarized together with new observations that led to propose new interpretations especially for the COT structure. Seismic line 1555 crosses central part of the Liwan sub-basin whereas seismic line 1530 captures only its southwestern edge. The Liwan sub-basin shows a thick Cenozoic post- to syn-rift succession reaching a thickness of 3.5 s TWT in its central part. The large-scale basin architecture is characterized by a large-scale low angle extensional fault on the northwestern boundary of the basin (at 10 km Fig. 3-4). Seismic line 1555 shows contrasting sedimentary package morphologies at the base of the syn-rift sequence (Tg-T70 interval Fig. 3) delimiting several sub-basins bounded by oceanward dipping low angle extensional faults, which soles out on different decoupling levels (Lei et al. 2019, Zhang et al., 2019). A strong amplitude reflector is well imaged at about 9 s TWT inboard and is interpreted as the Moho reflection. The continental basement is extremely thinned in the Liwan sub-basin (2.5 s TWT from Tg to the Moho) locally reaching only 8 km of thickness in some area (Wang et al., 2018). Notably, the early Cenozoic Wenchang formation (early/mid Eocene ~56-40 Ma) known from the more proximal basins is not clearly recognized in the deep Liwan sub-basin (Haizhang et al., 2017). In contrast, the main rifting phase of this basin is interpreted as middle Eocene to early Oligocene (Larsen et al., 2018d) suggesting that the Liwan sub-basin resulted mostly from the main, second rifting event affecting the PRMB. The syn-rift sedimentary package presents locally small flexures (<10 km wide, at 50-75 km Fig. 3) interpreted by Clift et al., (2015) to result from increased lower crustal flow induced by sediment loading. Alternatively, (Zhang et al., 2019) suggested that magmatic intrusions with possible laccolith geometries (at 20 km and 50 km Figs. 3-4) might be present and responsible for these small flexures.

Despite some significant morphological variations of the OMH in our two seismic profiles, it generally corresponds to a basement high, with Tg being 2-3s TWT shallower than within the Liwan sub-basin. The major intra-crustal reflections observed below the Liwan sub-basin can be followed until the southeastern tip of the OMH at the depth of 7 to 8 s TWT. Interestingly, the Moho below the OMH is interpreted at 9.5-10 TWT, thus 0.5-1s deeper than below the Liwan sub-basin. The OMH shows significant along strike structural variation: In line 1555 (Fig 4.), the OMH shows a general dome shape while in line 1530 it consists of two basement ridges reaching the seafloor (Fig. 5, at 25 km & 50 km). These basement ridges form continuous structures on a WNW-ESE trend over 10 to 20 km observed on free-air gravity maps (Supplementary material 1). These highs are inferred to be continental basement possibly associated with local syn- or post-rift magmatic additions (Gao et al., 2015; Wang et al., 2006; Zhang et al., 2019).

On the OMH, at Site U1501 a hiatus of ~4Ma (24-28 Ma, Jian et al., 2019 Fig. 3) is observed and marked by the T60 reflector which corresponds to an unconformity dated at 24Ma. At Site U1505, T60 is not a sedimentary hiatus (Jian et al., 2018), but both drill sites show a distinct change in sediment facies from post-rift carbonate rich marine sediment above T60 to a finning upward clastic sedimentary sequence below T60 (Larsen et al., 2018c) (Fig. 3). The syn-rift package (T70-Tg interval) is offset by several high-angle normal faults verging either ocean- or continent-ward forming small syn-rift basins filled by clastic sedimentary sequences (Larsen et al., 2018a). The oldest age of this syn-rift sequence was obtained ~200 m above its base (Tg) and is dated at ~34 Ma (Larsen et al., 2018a). The syn-rift clastic sedimentary facies within Site U1501 are similar to the Eocene Enping formation composed of deltaic to shallow marine sandstone reported in the more proximal basins of the PRMB (Xia et al., 2018)(Fig. 3). Below the Tg reflector, well lithified pre-rift conglomeratic sandstones of unknown age were recovered at Site U1501 (Fig. 3). Close to Site U1501, Tg truncates low-amplitude sub-Tg reflectors, along with a strong contrast in the degree of lithification this support significant erosion prior to the deposition of the syn-rift sequence, and hence, the presence of a major hiatus (Larsen et al., 2018a).

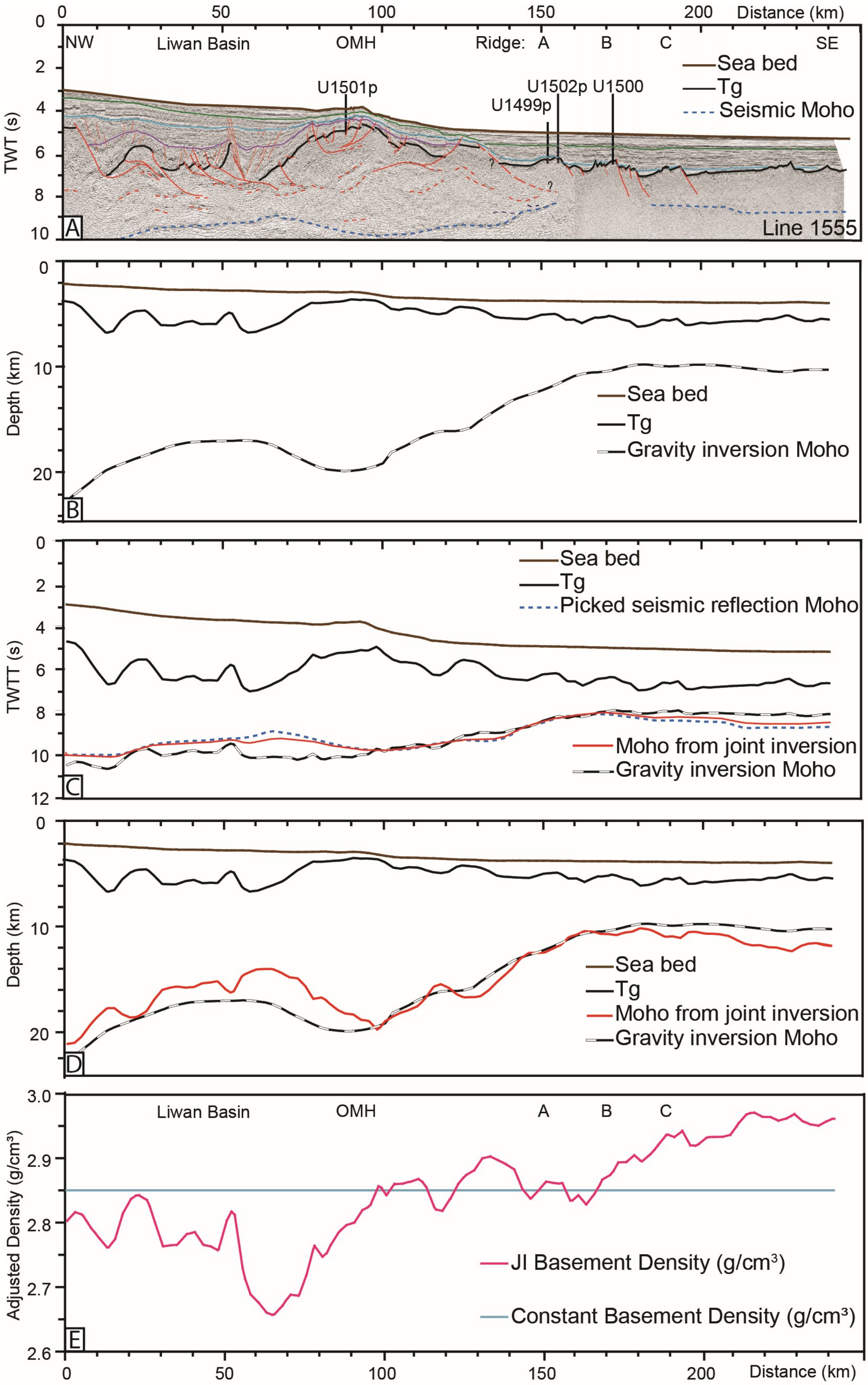

Figure 4: A) Seismic profile 1555 crossing the SE China COT modified from Larsen et al., 2018d (location of Line 1555 in Fig. 2). B) Depth converted Tg and Moho determined by 3D gravity

anomaly inversion. C) Time cross section comparing the Moho predicted from gravity anomaly inversion converted into time, the picked seismic Moho and the joint inversion Moho. D) Comparison in depth between the Moho determined by joint inversion and the Moho determined by gravity anomaly inversion. E) Lateral variations in basement density along the line 1555. The blue line corresponds to a density of 2.85 g/cm^3, which is the reference basement density used within the gravity anomaly inversion.

From the OMH to Ridge A the continental crust thins with the Moho rising from ~9 to ~7.5 s TWT. Continentward low angle extensional faults are observed in this area, but a major oceanward structure is interpreted at 135 km, offsetting Tg (Fig. 3). Ridge A is a ~10 km wide basement high, bounded by an oceanward dipping low angle extensional fault to the southeast. The Tg reflector at Ridge A shows low amplitude and variable continuity below which some reflectors indicate the presence of layered lithologies, possibly including sedimentary deposits. Ridge A (Figs. 2.b, 3) has been drilled at Site U1499 (Sun et al., 2018) on line 1530 and at Site U1502 (Larsen et al., 2018b) located 10 km to the east of line 1555. Site U1499 sampled post-rift, monotonous turbiditic sediments followed by a succession of lowermost Miocene and upper Oligocene fine-grained red clay, with strongly lithified pelagic red claystone (Sun et al., 2018). Below the red clay, the cored intervals recovered coarse siliciclastic sediments composed from top to bottom by a matrix supported breccia with angular and pebble-sized clasts, and a succession of very coarse-grained gravel, mostly consisting of cobble-sized clasts. All clasts represent previously eroded sedimentary rocks (mostly coarse-grained sandstone with some lithic fragments) (Fig. 3). The matrix supported breccia is deposited in a deep marine environment between 26 and 30 Ma and represents the earliest post-rift sedimentary unit. The origin of the lowermost gravel unit (pre 30 Ma) remains largely non-constrained as no depositional environment or age has been determined (Fig.3). It could be of early syn-rift age, but also of pre-rift age, but in any case a tectono-sedimentary shift occurred between these two units (Sun et al., 2018). Ridge A was also sampled 40 km to the East at Site U1502 and shows a post-rift succession similar to that of Site U1499. Below the post-rift succession, recrystallized dolomite related to hydrothermal processes alternates with claystone containing agglutinated benthic foraminifers suggesting an age as old as the late Eocene (Larsen et al., 2018d). The basement is made of highly altered MORB that suffered pervasive hydrothermal activity that in part extended into the lowermost overlying sediments (Larsen et al., 2018d), and hence, constrained basalt age to be more or less the age of the lowermost, hydrothermally altered sediments.

Ridge B (Fig. 2.b) is located 13 km southeastward of Ridge A and is a ~15km wide basement high. Its morphology is controlled by two main high-angle normal faults dipping oceanward, rotating top basement landwards, and displacing top basement by as much as 0.2s TWT (Fig. 3). Site U1500, located on Ridge B, cored deep marine pelagic sediments of Miocene to Oligocene age. These sediments overlie fresh MORB presenting pillow structures and intercalated sediments containing calcareous nannofossils indicating an Oligocene age (Stock et al., 2018). The marine magnetic anomaly C11n (30 Ma; Gee and Kent, 2007) mapped by (Briais et al., 1993) is closely aligned with Ridge B (Fig. 2). Based on clear sub-Tg seismic layering along a strike line through Site U1500, Larsen et al. (2018d) interpreted the volcanic edifice of MORB to extend to at least 2 km below Tg. The Moho reflection is absent below Ridge B along line 1555 (Fig. 3-8). However, in line 1530, a step in a better developed Moho reflection is observed between ridges A and B at 130 km (Fig. 5) and could correspond to the transition between “continental” and “oceanic” Moho. Locally on seismic sections, on top of the basement a thin and tilted sedimentary layer is observed related either to fault activity or to pelagic draping. This sedimentary layer was likely deposited during early Oligocene but no later than late Oligocene (Stock et al., 2018). With the exception of one fault bounded basin, no sedimentary fans are observed in relation with the faulting of Ridge B, suggesting a short time lag between basalt formation and faulting.

The most distal Ridge C (Fig. 2b) is located ~15 km further SE of Ridge B. It is characterized by rotated fault blocks bounded by oceanward dipping high-angle normal faults. Moho reflection reappears at this position around 8 s TWT on line 1555. The igneous nature of Ridge C has been confirmed by drilling at Site U1503 (Childress, 2019). As for Ridge B, the seismic data strongly suggests that the faulting took place shortly after the emplacement of the igneous rocks (Fig. 3).

The southeastern part of the two seismic sections (Fig. 4-5) presents a relatively smooth and flat Tg reflector parallel to the Moho reflection. These two reflectors are separated by 2 s TWT and show no major tectonic features as expected for oceanic crust. Marine magnetic anomalies C10n (Briais et al., 1993) dated at 28.7 Ma (Gee and Kent, 2007) is located slightly southeastward of Ridge C suggesting that MORB magmatism at this ridge has an age ranging between 30 Ma and 28.7Ma.

4.3) Gravity anomaly and joint inversions of gravity and seismic data

Line 1555

The Moho depth along seismic line 1555 has been determined using 3D gravity anomaly inversion using the interpreted depth converted sediment thickness from the seismic profiles (from seabed to Tg) (Fig. 4B). The resulting depth section (Fig. 4B) confirmed significant crustal thickness and architecture variations described previously from 1555 time section along the SE China margin. In this profile, the main depocentre of the Liwan sub-basin reaches up to 5 km of Cenozoic sediments overlying an 11 km thick continental basement. The crustal thickness below the OMH is around 16 km and progressively thins toward the COT and oceanic crust which show a thickness of 5 to 6 km (Fig. 4B). Notably, a shift in the Moho geometry occurs between ridges A and B at ~165 km passing from a gradual rise to a sub-horizontal geometry.

The Moho depth predicted from gravity inversion has been converted into the time domain for comparison with the Moho TWT interpreted from the seismic reflection data. A basement density of 2.85 $g.cm^{-3}$ is initially used in the gravity inversion (Chappell and Kusznir, 2008) (Fig. 4C). The crustal basement thickness from gravity inversion is converted into the time domain to give an interval TWT using a basement seismic velocity calculated using the velocity-density relationship ($V_p = 2.27\ \rho + 0.25$) described in section 3.2. This interval TWT is then added to the seismic interpretation of top basement in TWT to give the conversion of the gravity inversion Moho in depth into the time domain for direct comparison with the seismic Moho (TWT). As discussed earlier this allows the time converted gravity inversion Moho to be compared with the picked seismic Moho (Fig. 4C). The gravity inversion Moho below the Liwan sub-basin is on average 0.5s deeper than the picked seismic reflection Moho. From 110 to 180 km the seismic and gravity Mohos match well and from 180 km to the end of the line the gravity Moho is on average 0.3 s shallower than the seismic Moho. Joint inversion of the seismic and gravity data has been used to determine the combination of basement seismic velocities and densities required to match the Moho from gravity anomaly inversion with the picked Moho in the time domain. This matching of seismic and gravity Mohos results in a joint inversion Moho along profile 1555

(Figs. 4C, D). Figure 4E shows the lateral variation of the vertically averaged basement density resulting from the joint inversion. In comparison to the initial uniform basement density of 2.85 $g.cm^{-3}$, a deficit of mass below the Liwan sub-basin and an excess of mass oceanward of Ridge B are predicted by the joint inversion. Within the Liwan sub-basin the maximum deficit is 0.17 $g.cm^{-3}$ in the deepest part of the basin corresponding to a crustal basement density of approximately 2.73 $g.cm^{-3}$. This average deficit could be related to the crustal composition and to heterogeneities within basement. We suggest that in this case, the deficit of mass located below Tg in the Liwan sub-basin may be related to pre-Cenozoic sediments or stacked meta-sediments of the Yenshanian orogeny which effectively reduce the average density of the crust. Interestingly, any syn-rift magmatism, if at all present, is likely to be rather limited as it would push the average density upwards. On the OMH, crustal densities vary but are in average higher than the densities on the Liwan sub-basin and closer to the reference basement density of 2.85 $g.cm^{-3}$.

A major increase of estimated joint inversion densities occurs from 160 to 180 km on the profile 1555 (from ridges A to B), corresponding in depth section to a step of the Moho geometry (Fig. 4). Oceanward of this area, the average basement density rises to 2.93 $g.cm^{-3}$, which is close to the mean oceanic crust density of 2.89 $g.cm^{-3}$ (Carlson and Raskin, 1984). Therefore, we located the COB near 163 km where the density passes over 2.85 $g.cm^{-3}$, which likely corresponds to the formation of a new igneous crust.

Line 1530

We have applied the same procedure to line 1530 as for line 1555 (Fig. 5). The gravity inversion Moho is almost flat from 0 to 50 km at a depth of 21km (Fig. 5B). The influence of the two basement highs on the gravity inversion Moho is minor and limited to a Moho 1km deeper than under the adjacent basins. The Moho shallows progressively from ~20 km deep at the edge of the OMH to 10 km depth below Ridge B. The crust is 2 km thicker below Ridge A on this line than on line 1555. The entire oceanic domain is characterized by a constant Moho depth around 10 km and the crustal thickness ranges from 5 to 6.5 km thickness.

Conversion of the gravity inversion Moho to seismic reflection time (Fig. 5C) shows a deeper gravity Moho compared to the picked seismic Moho from 0 to 110 km except on the two basement highs of the OMH and Ridge A. It is notable that the seismic Moho TWT under the two basement highs is flat and shows no signs of velocity pull-up. From kilometre 110 onward the gravity inversion Moho is shallower than the picked seismic Moho. On the density profile (Fig5. E), the average crustal density until kilometre 110 is below the density used in the gravity anomaly procedure (2.85 $g.cm^{-3}$) except on the two basement high. This may imply that the continental crust is not a standard two layered continental crust, but has a composition that reduces the mean crustal density, which would be in agreement with a heterogeneous arc crust with nappe stacked, sedimentary basins and magmatic intrusions inherited from the Yenshanian orogeny. As a result, the Liwan sub-basin basement may partly be composed of metasediments whereas the OMH may contain denser magmatic intrusions. North-eastward along the margin, high density lower crustal bodies (Lester et al., 2014) are inferred to exist and suggests heterogeneity of the crustal layers. As for the section 1555, a major step in the density passing from below 2.85 to above 2.90 $g.cm^{-3}$ is located at the transition between ridges A and B and related to the COB.

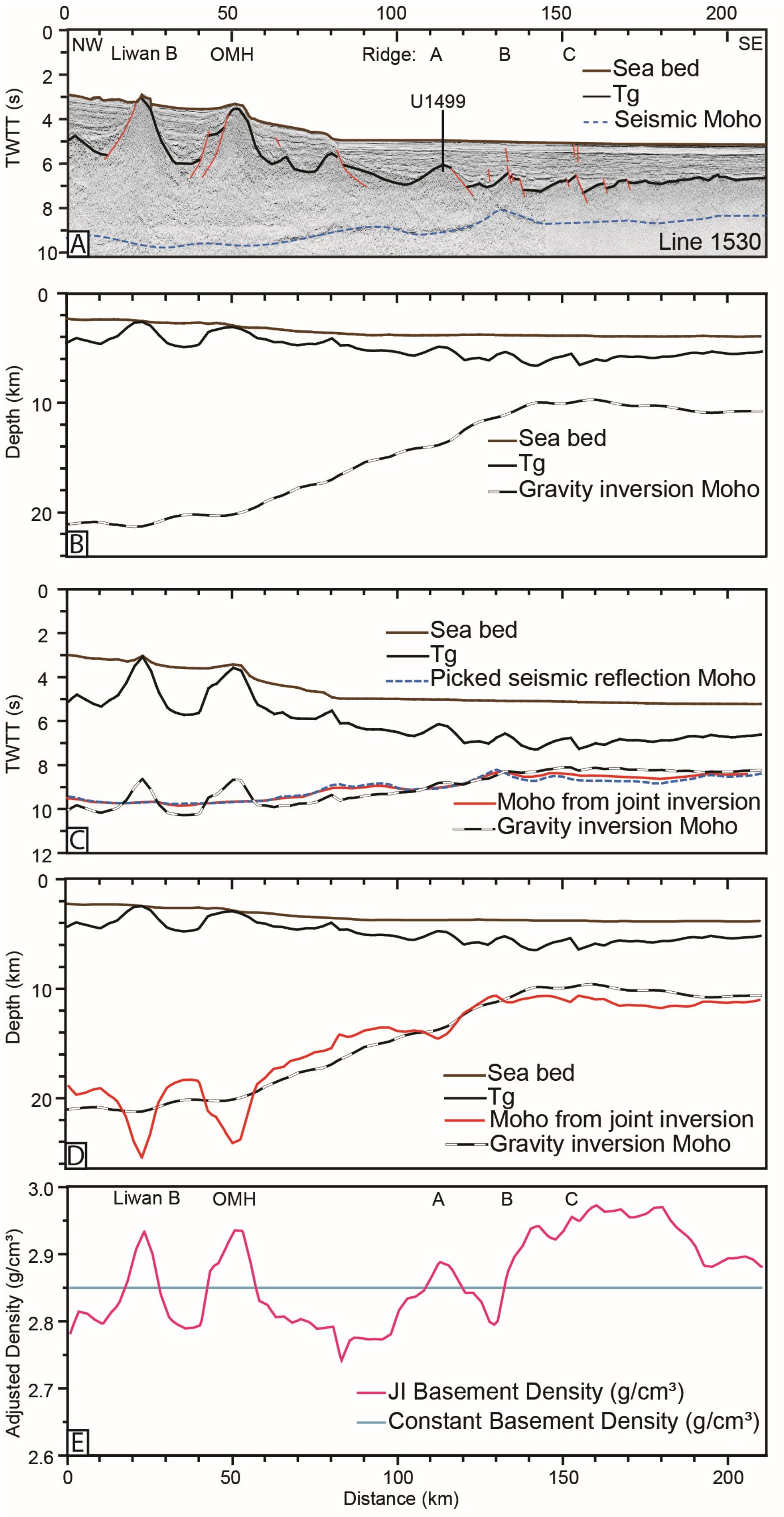

Figure 5: A) Seismic profile 1530 crossing the SE China COT (modified from Gao et al., 2015; Line location in Fig.2). B) Depth converted Tg and Moho determined by 3D gravity anomaly inversion. C)

Time cross section comparing the Moho predicted from gravity anomaly inversion converted into time, the picked seismic Moho and the joint inversion Moho. D) Comparison in depth between the Moho determined by joint inversion and the Moho determined by gravity anomaly inversion. E) Lateral variations in basement density along the line 1530. The blue line corresponds to a density of 2.85 g.cm^{-3}, which is the reference basement density used within the gravity anomaly inversion.

5) Architecture of the NW Palawan margin

5.1) Mapping of the rift domains

The NW Palawan margin is separated to the southwest from the Reed Bank by the Ulugan fault zone, which forms the northern boundary of the Borneo-Palawan trough (Fig. 6). To the northeast, the margin is bounded by a fault zone marking the western boundary of the domain affected by the eastward dipping subduction zone. The crustal thickness map (Fig.6A) highlights the differences in the thinning pattern of these three segments. The Dangerous Grounds constitute a wide zone (>300km) where the continental crust in general is thinned to less than 15 km with some narrow, SW-NE elongated ribbons of thicker crust (see Pichot et al., 2014; Gozzard et al., 2019). At the opposite, the Reed Bank is a massive basement high which thins rapidly toward the COT. On the NW Palawan margin, conjugate to the studied SE China segment, the proximal domain trends parallel to the coastline (Fig. 6), and the thinned domain is often separated from the COT domain by narrow structural highs as observed by Franke et al. (2011). The COT seems partly oblique to the marine magnetic anomalies suggesting an initially complex evolution. This is further suggested by the only sporadic and indirect indication of a possible presence of C11n (Fig. 6)(Briais et al., 1993), which is well defined on the SE China conjugate margin segment.

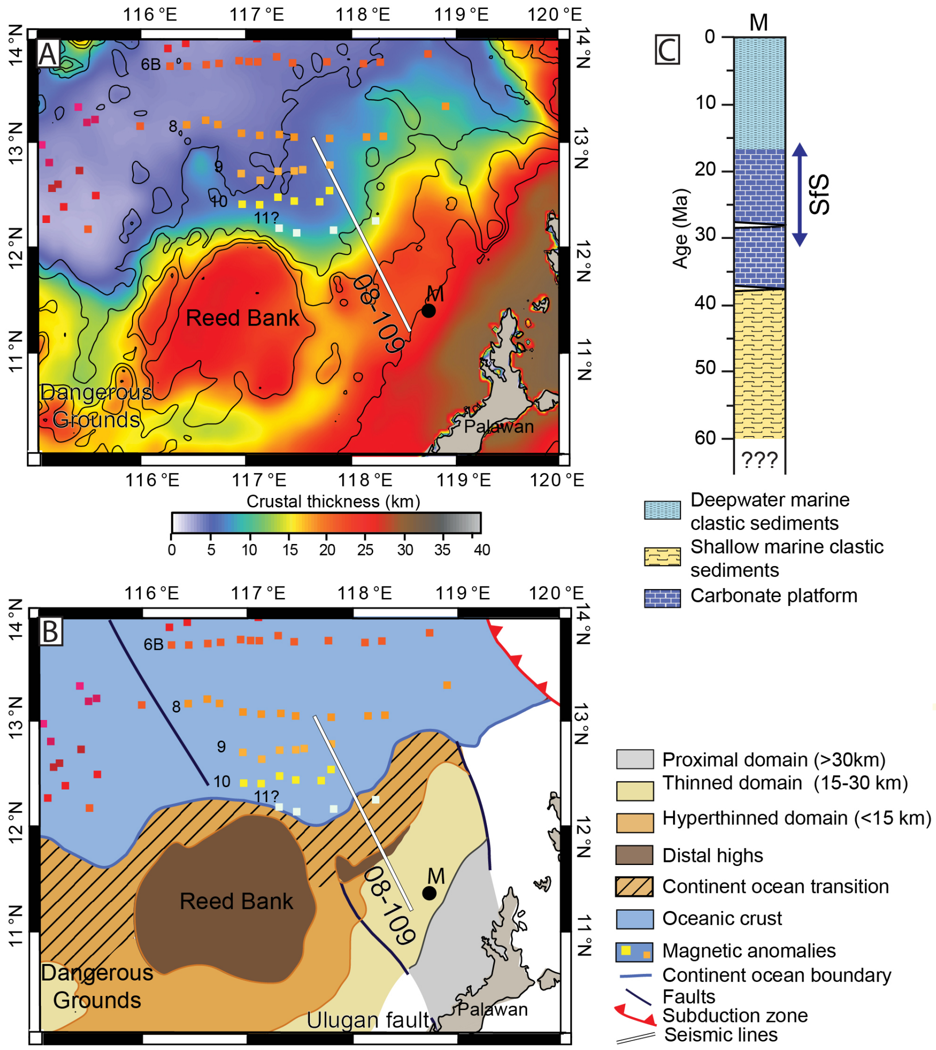

Figure 6: A) Crustal thickness map of the NW Palawan margin determined by 3D gravity inversion B) Map of the rift domains. Magnetic anomalies are from Briais et al., 1993. M: Malanpaya borehole. C) Synthetic stratigraphic columns of Northwest Palawan margin (based on the Malampaya borehole (Fournier et al., 2005). SfS: seafloor spreading.

5.2) Seismic description of line BGR08-109

The seismic line BGR08-109 (Fig. 7) crosses the NW Palawan margin on a segment described previously by Franke et al. 2011. Several structural domains have been identified in this margin: a wide inner basin (>50 km wide), the narrow Palawan structural high (PSH), the COT and the oceanic crust.

The inner basin is defined by a basement that is offset by a series of normal faults controlling thin wedge-shaped syn-rift sedimentary packages. This basin is thicker in its centre with top basement reaching a maximum depth of 5s TWT, and with sediment fill of ~2s TWT which is less than the Liwan sub-basin in the SE China margin. Laterally this inner basin passes into PSH showing a positive ~10 km wide bathymetric expression on the seabed. This high could be considered an analogue to the OMH on the SE China margin. This basement high is bounded by extensional structures, which forms an escarpment of 2s TWT. Seaward, a series of oceanward dipping normal faults is interpreted between 120-150 km (Fig. 7 A, B). The COT is bounded oceanward by an escarpment of the top basement. Seismic definition at the oceanward edge of the COT is partly obscured by volcanic edifices and sills within the post-rift sedimentary sequences. Discontinuous and Moho-like reflections are observed within COT domain, but the quality of seismic data precludes further characterization of deep crustal structures as well as a good definition of syn-rift structures.

From 90 to 0 km, the top basement reflector is observed at 6.8 s TWT and another deeper reflector interpreted as the Moho reflector is observed at 9 s TWT, both reflectors are sub-horizontal and parallel. In addition, this domain contains marine magnetic anomalies C10n and C9n. Altogether, this domain is interpreted as oceanic. A sporadic presence of magnetic anomaly C11n is suggested close to the interpreted COB (Fig. 6) by analogy with the SE Chinese side. However, as stated by Briais et al., (1993) the identification of anomaly C11n is not clear on this southern side of the SCS and has also been discarded from the global oceanic magnetic anomaly repository (Seton et al., 2014).

The stratigraphic record of the distal Palawan margin remains poorly constrained because of the lack of deep drill holes on the outer margin. Nevertheless, based on seismic facies combined with wells on the shelf, a general stratigraphic framework is suggested. Contrasting with the SE China margin, early post-rift Nido platform carbonates characterized by bright sub-parallel reflections (Fig. 7) (i.e. Nido formation, Steuer et al., 2013) are identified across the proximal part of the profile and suggested on the COT. While syn-rift sedimentary thickness within the inner basin of the NW Palawan margin is significant, in the COT it is reduced to small fault bounded basins (Figs. 7, 8).

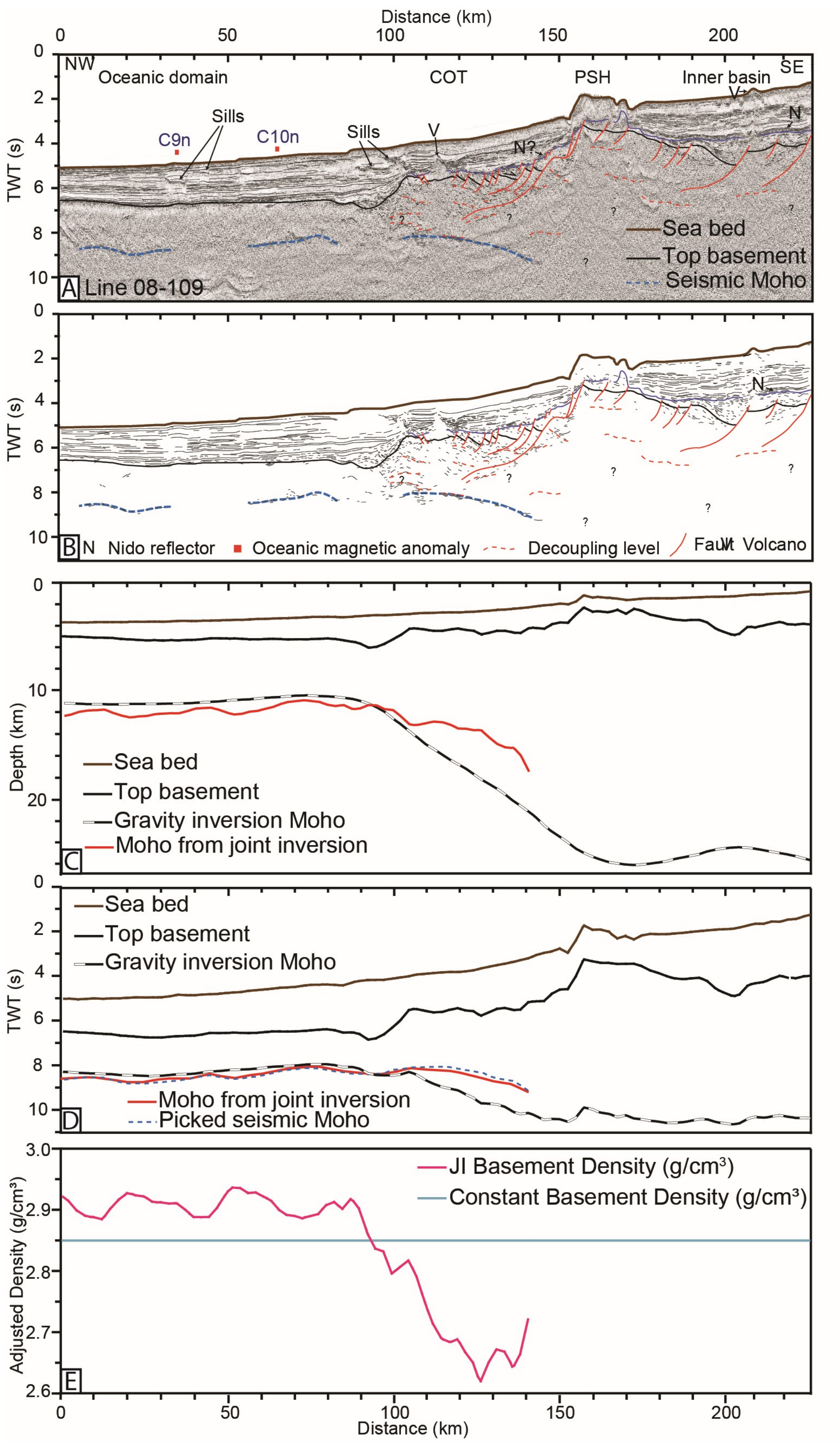

Figure 7: A) Seismic section BGR08-109 interpreted with the major horizons and unconformities (modified from Franke et al., 2011). B) Line drawing of the seismic section C) Depth converted top

basement and comparison in depth between the Moho determined by joint inversion and the Moho determined by gravity anomaly inversion. D) Time depth cross section comparing the Moho predicted from gravity anomaly inversion converted in time, the picked seismic Moho and the joint inversion Moho. E) Lateral variations in basement density along the line 08-109. The blue line corresponds to a density of 2.85 g.cm^{-3}, which is the reference basement density used within the gravity anomaly inversion. PSH: Palawan structural high.

5.3) Gravity inversion of line BGR08-109

We performed gravity inversion and joint inversion on profile 08-109. However, as no reliable Moho reflection is identifiable inboard of kilometre 140 we only perform joint inversion for the COT and oceanic domain (Fig. 7). The Moho from gravity inversion below the inner basin is around 24 km deep, but is slightly shallower within the deepest part of the inner basin. The PSH marks the onset of the main thinning of the continental crust between 90 and 155 km. The sharp deepening of the top basement observed on the seismic section oceanward of the PSH corresponds to a gradual shallowing of the Moho over the whole COT. From kilometre 0 to 80 the Moho is almost flat at a depth of 10-11 km forming a crustal layer of 6 to 7 km consistent with its interpreted oceanic nature. The continentward deepening of the Moho around kilometre 90 is confirmed by the basement density estimation resulting from joint inversion of gravity anomaly and TWT seismic data (Fig. 7E). The position of the COB is around kilometre 95 based on the density above 2.85 g.cm^{-3} towards the northwest, whereas continentward within the COT domain the average basement density is only 2.72 g.cm^{-3}. This density is low compared to our reference basement density (2.85 g.cm^{-3}). This might be explained in various ways: (1) Rifting developed within an older, deep sedimentary basin, (2) errors in the interpretation of the seismic top basement, or/and Moho reflectors. Indeed, if seismic top basement is picked too shallow, “light” sediments are integrated into the gravity in inversion and the average crustal thickness is reduced. Similarly if Moho is picked too deep its average density is reduced.

6. Discussion

6.1) Conjugate margins architecture

The combination of gravity inversion and interpretation of high quality seismic data constrained in critical locations by deep boreholes has allowed us to: (1) confidently tie together the two conjugate margins along the original line of breakup; and (2) amend a definition of structural domains based on crustal structures. The results show that the conjugate segments of the SE China and the NW Palawan margins in pre-breakup time (pre ~30 Ma) together formed a very wide (600 km) rifted zone. This wide rift zone formed a "pinch and swell" crustal architecture (e.g. Savva et al. 2014, Clerc et al. 2018) characterized by a succession of thinned to hyper-thinned basins (e.g. Liwan and Baiyun sub-basins on the SE China margin) separated by basement highs (Fig. 8). The line of final breakup partitioned this wide rift zone into a ~400 km wide margin in the north, and a ~200 km wide margin in the south.

At the SCS rifted margins, several studies suggest decoupling between a brittle upper crust and a thick, ductile lower crust (Brune et al., 2017; Savva et al., 2014). This rheological layering of the crust may be caused by several parameters, such as the composition of the crust (more felsic, less mafic, Brune et al., 2017, Nagel and Buck, 2007), structural softening by tectonism, inherited differences in crustal strength (Duretz et al., 2016) and the temperature at Moho level (hotter due to thinner continental lithosphere, Nagel and Buck, 2007). Interestingly, within the SE China and NW Palawan margins, based on seismic interpretation we suggest multiple decoupling levels at various depths (e.g., red dashed lines Fig. 3, 25-100 km, Fig.7, 95-160 km). These surfaces may reflect inheritance of pre-rift structural and lithological differences that continue to control weak and strong zones. Variable pre-rift rheological structure is most likely because Paleogene SCS rifting developed within a complex crust that suffered strong deformation during the Mesozoic. The Mesozoic setting is characterized by a convergent system (Holloway, 1981; Klimetz, 1983; Li and Li, 2007; Taylor and Hayes, 1983) associated with wide occurrence of granites (J. Li et al., 2014; Savva et al., 2014), volcanoclastic sediments (Nanni et al., 2017), strongly lithified conglomerates (IODP Site U1501), green-schist facies metamorphic rocks (IODP Site U1504 (Larsen et al., 2018c), and metasedimentary rocks (Kudrass et al., 1986) dredged or drilled on the SCS margins. Strongly folded Mesozoic sedimentary formations visible on seismic sections (on the Dongsha High, Li et al., 2008), and outcrop on Northern Palawan Island (Faure et al., 1989) are evidence of pre-Cenozoic thrusting and folding within the rift basement below the Tg reflector. The occurrence of multiple decoupling levels at variable depth as observed on seismic data (Fig. 3, 7, 8) may be inherited from a Mesozoic "Andean-type” margin characterized by the former arc, nappes, suture zones and an accretionary wedge.

In addition, the joint inversion of gravity modelling highlights variation of densities along the seismic profiles of the SE China margin. On line 1555, the south-eastern part of the OMH has crustal densities in the range of the reference density (2.85 $g.cm^{-3}$), whereas densities below the Liwan sub-basin are lower. The Liwan sub-basin basement may therefore comprise meta-sediments. By contrast and in accordance with our modelling, numerous structural highs have been interpreted as former Mesozoic plutonic complexes of arc origin and suggesting that major basin bounding faults formed at the edge of Mesozoic intrusive bodies (Savva et al., 2014). Petri et al., (2019) using thermo-mechanical modelling demonstrated the potential importance of such initial heterogeneities in the continental lithosphere on the control of the architecture/development of extensional deformation at rifted margins. In addition to mechanical inheritance, the thermal state of the lithosphere possibly also impacted the rifting of the SCS margins. Indeed, the emplacement of granites between 107-86 Ma (Li et al., 2014) took place less than 50 Ma before the onset of Cenozoic rifting implying a thermally non-equilibrated lithosphere prior to rifting event (McKenzie, 1978). The pre-rift geothermal gradient remains unconstrained, but regarding the fact that the rifting of the SCS developed in a post-orogenic context, it suggests similar heat flow to the one currently observed in the Basin and Range (Western US) 85±10 mW/m^2 (Blackwell, 1983). By comparison the continental heat flow average is much lower 57 ±10 mW/m^2 (Sclater et al., 1980). This combination of a strongly heterogeneous continental lithosphere combined with elevated thermal conditions probably resulted in a weak pre-rift crust with multiple decoupling zones (interpreted on Figs 3, 7, 8), and a ductile lower crust that framed the final architecture of the margin.

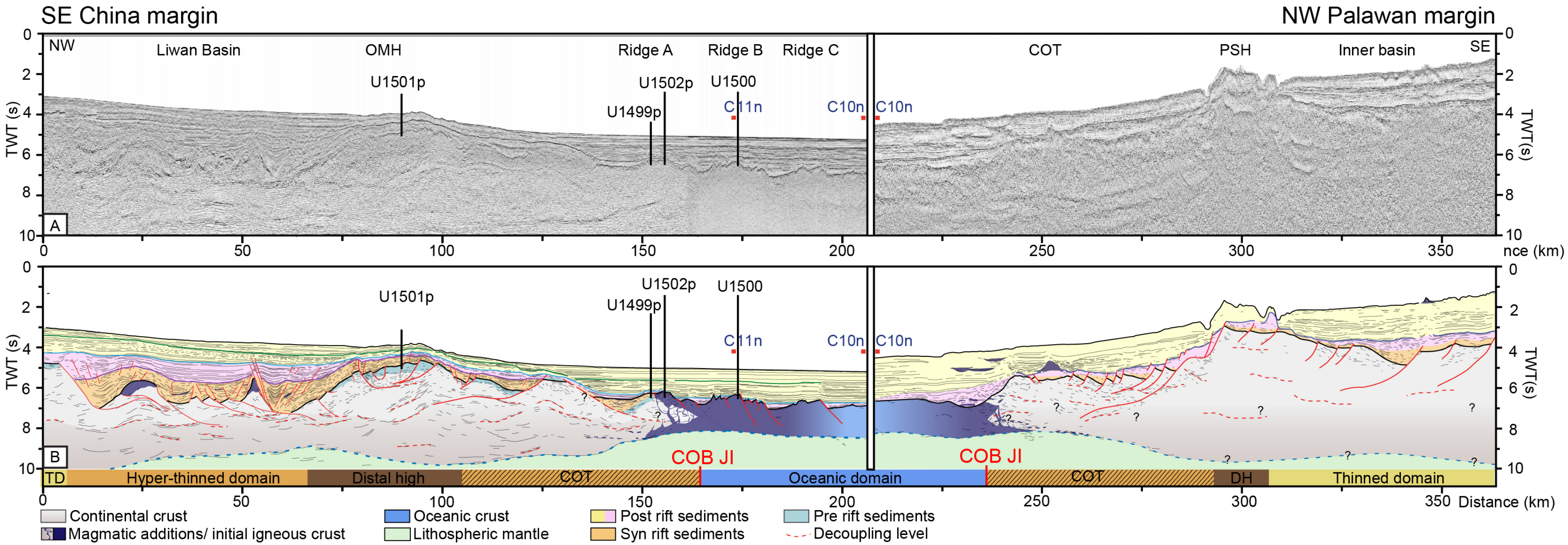

Figure 8: Conjugate seismic cross sections of the SE China-NW Palawan conjugate margins (Larsen et al., 2018e; Franke et al., 2011). A) Un-interpreted section 1555 and 08-109 cropped and merged at the magnetic anomaly C10. B) Conjugate margins seismic interpretation

6.2) Tectonic and magmatic processes shaping the COT and initial igneous crust on the two conjugate margins. JI, joint inversion.

The COT along the SE China margin corresponds to a ~60km wide domain from 110 to 170 km (Line 1555, Fig.8) where the gravity inversion Moho shallows from 20 to less than 10 km (Figs. 4-5). We interpret a major oceanward dipping low angle extensional fault at 130-155 km (Line 1555, Fig.8) offsetting the top basement by 0.8 s (TWT). Over the same interval, the seismic Moho depth abruptly shallows from 9 to 7.5 s (TWT). Hence, we interpret Ridge A (150-160 km) as the hanging-wall block above this major low angle extensional fault. IODP drilling results show that this ridge has a composite nature. At Site U1502 the top basement is formed by late Eocene to early Oligocene altered MORB whereas at Site U1499 pre- and/or syn-rift sediments are found below Tg (Larsen et al. 2018d). Importantly the continental Moho can be followed continuously from the OMH to Ridge A on lines 1555 and 1530 showing that Ridge A is at least partly made by highly thinned continental basement (<7km thick), but also affected by breakup magmatism (IODP Site U1502, Larsen et al., 2018b). This interpretation is also supported by the joint inversion of gravity and seismic data on both seismic sections showing that the average basement density at Ridge A is in the range of continental crust (2.85 $g.cm^{-3}$) (Fig. 4-5).

From Ridge B to the end of the seismic line, the joint inversion shows basement density above 2.85 $g.cm^{-3}$ (Fig. 4-5). The domain between ridges A and B is interpreted as the transition from continental crust intruded by magmatic additions (Ridge A) to an entirely mafic igneous crust (Ridge B) and defines a sharp COB. This COB is placed exactly at the same place on the landward side of Ridge B on both seismic lines 1555 and 1530. Line 1530 in this position shows a local, narrow shallowing of the Moho reflector (Fig. 4, around 130 km). The location of the COB, deduced from geophysical data, is consistent with coring results from Site U1500 on Ridge B, which sampled fresh pillow basalts and flows with MORB composition (Stock et al., 2018). As a result, along our profile, the COT is characterized by highly thinned continental crust associated with progressive emplacement of MORB-type magmatic additions. The COB represents the oceanward end of the COT identified with a <4km distance uncertainty by combining gravity modelling, seismic interpretations and core data. Given this relatively sharp boundary a binary definition of COB can be applied (Eagles et al., 2015).

The oceanic nature of Ridge B is in agreement with the close alignment of magnetic anomaly C11n (30 Ma). Ridges B and C (Fig.9) both show landward block rotation along ocean ward dipping high angle normal faults. These offset the igneous basement to form small half-graben basins filled by post-rift sediments. Sediment fill, however, show poorly developed or no wedge-shaped geometries, and the T60 reflector is not faulted (Fig. 9). These observations suggest that faulting at Ridges B and C occurred while or slightly after basaltic emplacement (C11n, 30Ma) and before the T60 unconformity (This unconformity at Site U1501 corresponds to a sedimentary hiatus from ∼24 Ma to ∼28 Ma (based on biostratigraphy) or ∼30 Ma (based on Sr-isotope stratigraphy) Jian et al. 2019). The rooting level of these normal faults is likely in the deep lower crust (ocean layer 3).

On the NW Palawan margin, the Moho shallows oceanward from a depth of 24 to 11 km in about 70 km (Fig. 7). The top basement deformation within the COT is characterized by a set of closely spaced oceanward dipping faults likely rooting in shallow crustal decoupling levels. The fault dip and the structural style may represent the antithetic counter part of the major low angle extensional fault interpreted on the SE China side (km 135; Fig. 8). In contrast with SE China, in the NW Palawan margin the magnetic anomaly C11n (30.0 Ma) is not clearly defined (Briais et al. 1993), but seems to project to the location of the COB on line BGR08-109 (See map Fig.6). However, the first firmly observed magnetic anomaly on both margins is C10n (28.7 Ma) and is located ~45 km from the COB at the SE China margin, and at ~35 km from the COB at the Palawan margin. Another important difference is that this oldest igneous crust off the NW Palawan margin is not faulted, in strong contrast to the faulted Ridges B and C of the SE China margin. Hence, we observed two types of asymmetry: 1) the asymmetrical deformation pattern of the two conjugate highly thinned continental margins (Fig. 8), and 2) the width and morphological asymmetry of the initial igneous crust (Fig. 9)

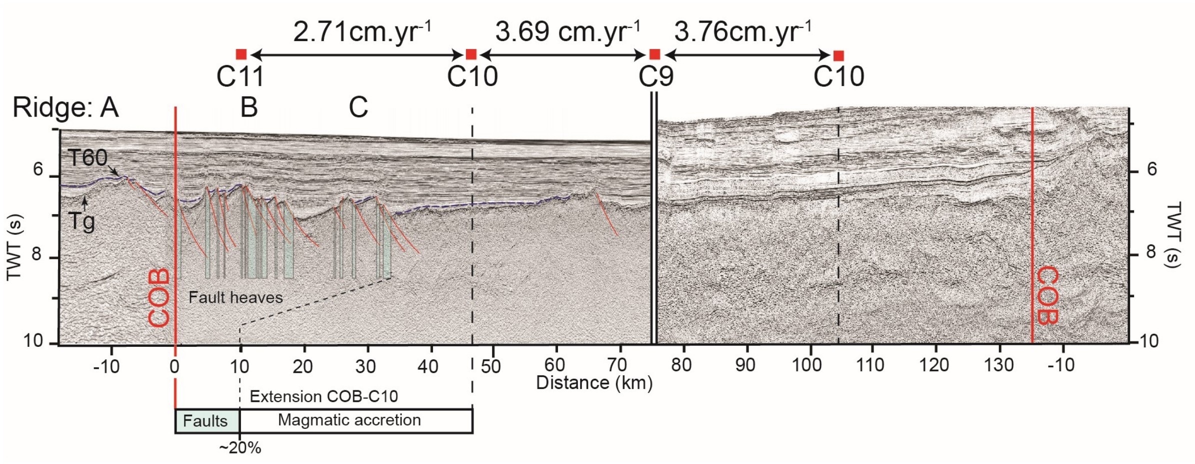

Figure 9: Conjugate seismic cross sections of SE China-NW Palawan conjugate margins cropped and accolated at C9 (~27.97 Ma). The faults heaves are added together in order to get the ratio between tectonic faulting and magmatic extension from COB to C10

6.3 Evolution of the SE China-NW Palawan breakup and initial oceanic accretion

6.3.1) Stage 1: Eocene-Oligocene boundary: Extreme thinning of the continental lithosphere and related magmatism ~34 -30 Ma

The final rifting stage in the SE China-NW Palawan conjugate margins occurs during the latest Eocene as emphasized by borehole data calibrated with seismic interpretations (Larsen et al., 2018d). Seismic interpretation suggests that the final extension is caused mainly by a low angle extensional fault located on the SE China margin (Line 1555, km 130-155), which enhanced decompression melting. Although in this stage, the continental crust is less than <10 km thick, the seismic data do not allow the determination of whether the low angle extensional fault is soling onto an internal crustal level like in the more proximal basins (e.g. Liwan) or in the uppermost mantle. This structure is interpreted to accommodate extension triggering an asymmetric crustal architecture at the edge of the COT (Fig. 10), similarly to that of the hyper-thinned basins observed on both margins (e.g. Liwan sub-basin). Overall and similarly to the observation from the Red Sea breakup (Ligi et al., 2018), the extreme lithospheric thinning resulted in the initiation of MORB magmatism before continental rupture. From seismic observations and IODP drilling, we interpret Ridge A as representing the last continental rotated fault block strongly overprinted by magmatic additions emplaced through the whole residual crust. Basalts and the first (~5m) early Oligocene sediments of Site U1502 show significant hydrothermal alteration. This alteration constrains the timing of magmatic activity and faulting to early Oligocene time (34-30 Ma). The concomitant faulting and magmatic activity results in the continental crust tapering with rapid but likely progressive replacement by magmatic rocks. The COTs on both margins appear quite narrow and formed most likely in less than 4 Ma by faulting, diking, intrusions and building of volcanic edifices (Larsen et al., 2018d).

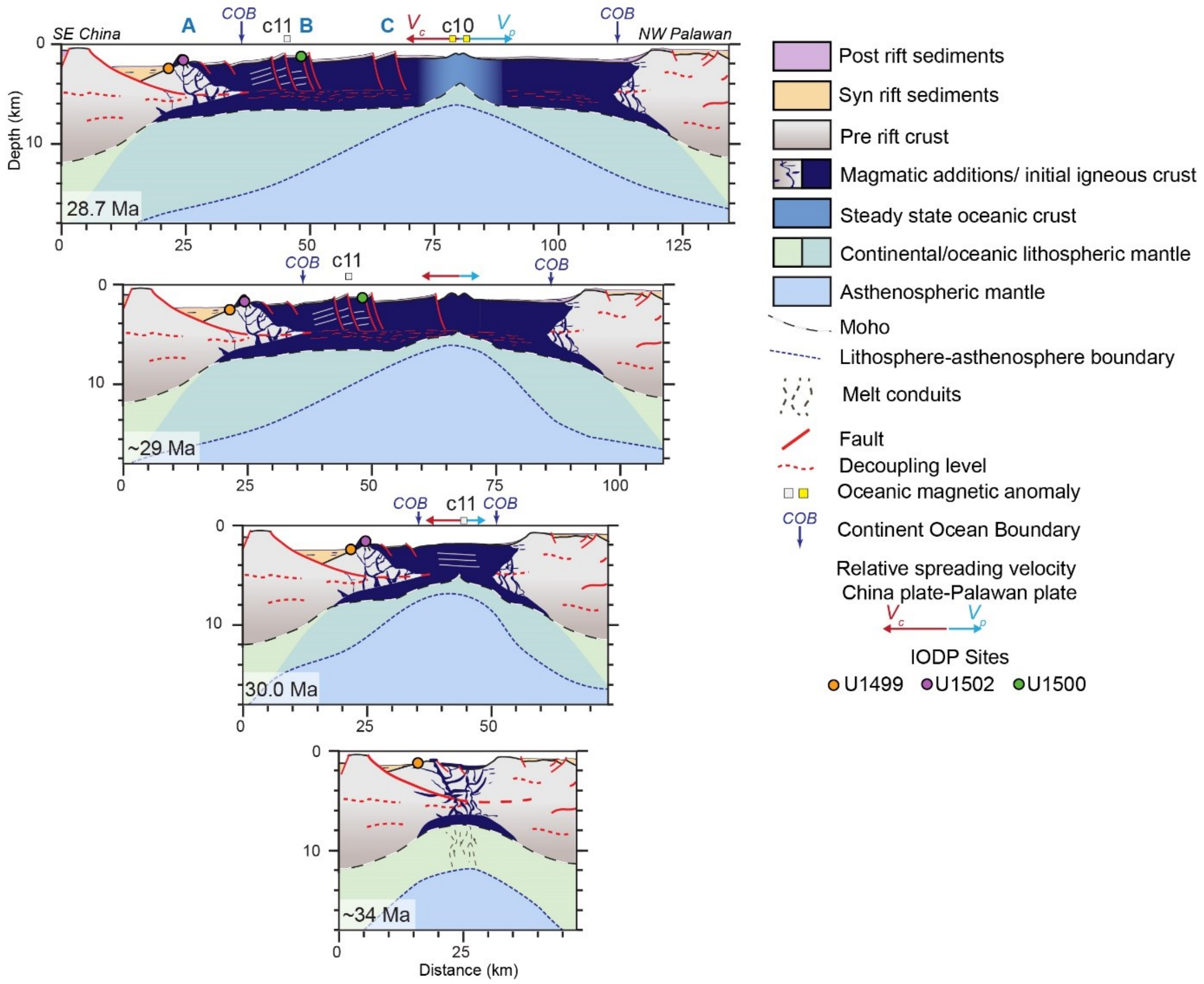

Figure 10: Tectono-magmatic evolutionary model illustrating the breakup and the early seafloor spreading at the SE China-NW Palawan conjugate margins. The initial asymmetric spreading and the strong interplay between faulting and magmatism are highlighted.

6.3.2) Stages 2 and 3: Formation of initial igneous crust ~30 – 29 Ma

Seismic interpretation, borehole data and gravity modelling highlight the asymmetry in width and morphology of the initial igneous crust between SE China and NW Palawan. The morphology and ages of the T60 reflector (Fig. 9) indicate that this asymmetry is produced within a short time interval after the formation of the igneous crust and therefore likely generated during seafloor accretion. The calculated half-spreading rate between C11 and C10 is 2.71 $cm.yr^{-1}$ and accelerates to 3.69 $cm.yr^{-1}$ between C10 and C9 on the SE China side. C11 is not clearly identified on the NW Palawan margin (Fig. 6), therefore half-spreading rate cannot be determined, but as the distance is smaller between the COB and C10 compared to the SE China side the half-spreading rate is slower on the NW Palawan, implying that initial spreading was asymmetric. However, the sum of the fault heaves between the COB and C10 on the SE China side represent a minimum of 20% of the total distance while the remaining 80% are caused by magmatic accretion (Fig. 9). If we remove the 20% caused by extensional faulting to the distance between the COB and C10 on the SE China margin, the distance between the COB and C10 becomes similar on both margins (Fig. 9). An explanation to this asymmetry could be related to a southward jump of seafloor spreading axis, which would be consistent with the younger igneous crust observed on the conjugate Palawan margin. However, all faults on the SE China margin dip oceanward and there is no seismic evidence of an extinct axis (e.g., a symmetric graben structure) making the axis jump hypothesis unlikely. This analysis supports a southward migration of the initial spreading centre with tectonic extension within the trailing edge (on SE China side compared to the mobile Palawan block see Stein et al., 1977).

The stage of asymmetric spreading ended around C10n when spreading rate became symmetric without normal faulting, and accelerated to ~3.7 $cm.yr^{-1}$ (Fig. 9). Asymmetric seafloor spreading is commonly observed on oceanic basins (Müller et al., 2008), however the 20% observed on our example is anomalously high. One reason for an initial asymmetric spreading stage might be related to a temporary, preferred shape of asthenospheric upwelling, less inclined towards the northwest inducing a faster extension of the trailing edge (Stein et al., 1977). This asthenospheric upwelling could be related to the asymmetric late stage of rifting (e.g. faulting of Ridge A) resulting in a migration of the deformation and magmatism (Brune et al., 2014). We interpret the phase between ~30 Ma and C10 as the incipient building of a symmetric steady state oceanic accretion.

6.3.3) Stage 4: Steady-state oceanic accretion ~28.7 Ma onward

Between anomalies C10n and C9n the half spreading rate are similar on both side (3.69 $cm.yr^{-1}$ on the SE China margin and 3.76 $cm.yr^{-1}$ on the NW Palawan Fig. 9) suggesting a steady-state symmetric oceanic crust accretion (Fig. 10). Oceanward of C10n the oceanic seismic facies are very similar on both sides of the SCS with little faulting of the top of the oceanic crust suggesting a magma dominated accretion. The symmetric steady state oceanic spreading system starts around C10n (28.7 Ma) (Fig. 10; Briais et al., 1993) and corresponds to the stabilization of the plate boundary until the southward jump identified at the C6b (~23 Ma) (Briais et al., 1993).

7. Conclusion

This study investigated the architecture of SE China-NW Palawan conjugate margins within the eastern SCS sub-basin using information from new IODP drill cores, high quality seismic sections and modelling of the free-air gravity anomalies. The localisation of the COB is accurately determined by gravity inversion and is in agreement with the IODP drill cores and seismic profiles.

On the continental rifted margins, gravity inversion highlights variations of crustal densities and seismic interpretations suggest multiple decoupling levels which influence the extensional deformation style. Such crustal heterogeneities are considered to be related to the structural, compositional and thermal inheritance from the Mesozoic convergence history. Our study unravels the architecture of the COT on the SE China-NW Palawan conjugate margins. Both COTs show normal faults and hyperthinned crust (<15 km) over equivalent distances until the COB, however, the final crustal thinning is suggested to be accommodated by a major low angle extensional fault locate on the SE China margin. The strong lithospheric thinning induced the emplacement of MORB magmatic additions within the COT. This initial magmatic activity was concomitant with continued deformation of continental crust until the COB. Oceanward of the COB the initial igneous crust along the two conjugate margins is asymmetric in both width and morphology. These observations constrained by seismic stratigraphy, suggest that initial spreading rate was faster on the SE China side before oceanic magnetic anomaly C10n (28.7 Ma) by which time the spreading ridge generated oceanic crust at symmetric rates. The initial asymmetry pictures the incipient building of a steady state oceanic spreading and could be due to oriented asthenospheric upwelling inherited from the asymmetric late rifting stage.

Acknowledgments

This research used data provided by the International Ocean Discovery Program (IODP).We thanks the participants to IODP Expedition 367-368 as well as the captains and crew of the Joides Resolution. We acknowledge IODP France for post cruise support. Funding for this research and access to industrial seismic and borehole data were provided by Total SA R&D (J.N. Ferry). We are grateful to the Editor Tiago Alves. Chao Lei, William Bosworth and two anonymous reviewers are thanked for their helpful suggestions and comments.

References

Alvey, A., Gaina, C., Kusznir, N.J., Torsvik, T.H., 2008. Integrated crustal thickness mapping and plate reconstructions for the high Arctic. Earth Planet. Sci. Lett. 274, 310–321. https://doi.org/10.1016/j.epsl.2008.07.036

Amante, C., Eakins, B.W., 2009. ETOPO1 1 Arc-Minute Global Relief Model: Procedures, Data Sources and Analysis. https://doi.org/10.7289/V5C8276M

Arfai, J., Franke, D., Gaedicke, C., Lutz, R., Schnabel, M., Ladage, S., Berglar, K., Aurelio, M., Montano, J., Pellejera, N., 2011. Geological evolution of the West Luzon Basin (South China Sea, Philippines). Mar. Geophys. Res. 32, 349–362. https://doi.org/10.1007/s11001-010-9113-x

Barckhausen, U., Engels, M., Franke, D., Ladage, S., Pubellier, M., 2014. Evolution of the South China Sea: Revised ages for breakup and seafloor spreading. Mar. Pet. Geol. 58, 599–611. https://doi.org/10.1016/j.marpetgeo.2014.02.022

Birch, F., 1961. The velocity of compressional waves in rocks to 10 kilobars, part 2. Elastic Prop. Equations State 66, 91–116. https://doi.org/10.1029/SP026p0091

Blackwell, D.D., 1983. Heat flow in the Northern Basin and Range Province, in: The Role of Heat in the Development of Energy and Mineral Resources in the Northern Basin and Range Province. pp. 81–93.

Boillot, G., Winterer, E.L., Meyer, A.W. (Eds.), 1987. Proceedings of the Ocean Drilling Program, 103 Initial Reports, Proceedings of the Ocean Drilling Program. Ocean Drilling Program. https://doi.org/10.2973/odp.proc.ir.103.1987

Briais, A., Patriat, P., Tapponnier, P., 1993. Updated interpretation of magnetic anomalies and seafloor spreading stages in the south China Sea: Implications for the Tertiary tectonics of Southeast Asia. J. Geophys. Res. Solid Earth 98, 6299–6328. https://doi.org/10.1029/92JB02280

Brocher, T.M., 2005. Empirical Relations between Elastic Wavespeeds and Density in the Earth's Crust. Bull. Seismol. Soc. Am. 95, 2081–2092. https://doi.org/10.1785/0120050077

Brune, S., Heine, C., Clift, P.D., Pérez-Gussinyé, M., 2017. Rifted margin architecture and crustal rheology: Reviewing Iberia-Newfoundland, Central South Atlantic, and South China Sea. Mar. Pet. Geol. 79, 257–281. https://doi.org/10.1016/j.marpetgeo.2016.10.018

Brune, S., Heine, C., Pérez-Gussinyé, M., Sobolev, S. V., 2014. Rift migration explains continental margin asymmetry and crustal hyper-extension. Nat. Commun. 5, 4014. https://doi.org/10.1038/ncomms5014

Cameselle, A.L., Ranero, C.R., Franke, D., Barckhausen, U., 2017. The continent-ocean transition on the northwestern South China Sea. Basin Res. 29, 73–95. https://doi.org/10.1111/bre.12137

Carlson, R.L., Raskin, G.S., 1984. Density of the ocean crust. Nature 311, 555–558.

https://doi.org/10.1038/309126a0

Chappell, A.R., Kusznir, N.J., 2008. Three-dimensional gravity inversion for Moho depth at rifted continental margins incorporating a lithosphere thermal gravity anomaly correction. Geophys. J. Int. 174, 1–13. https://doi.org/10.1111/j.1365-246X.2008.03803.x

Childress, L., 2019. Expedition 368X Preliminary Report: South China Sea Rifted Margin, International Ocean Discovery Program Preliminary Report. International Ocean Discovery Program. https://doi.org/10.14379/iodp.pr.368X.2019

Clerc, C., Jolivet, L., Ringenbach, J.C., 2015. Ductile extensional shear zones in the lower crust of a passive margin. Earth Planet. Sci. Lett. 431, 1–7. https://doi.org/10.1016/j.epsl.2015.08.038

Clerc, C., Ringenbach, J.C., Jolivet, L., Ballard, J.F., 2018. Rifted margins: Ductile deformation, boudinage, continentward-dipping normal faults and the role of the weak lower crust. Gondwana Res. 53, 20–40. https://doi.org/10.1016/j.gr.2017.04.030

Clift, P.D., Brune, S., Quinteros, J., 2015. Climate changes control offshore crustal structure at South China Sea continental margin. Earth Planet. Sci. Lett. 420, 66–72. https://doi.org/10.1016/j.epsl.2015.03.032

Cowie, L., Angelo, R.M., Kusznir, N., Manatschal, G., Horn, B., 2017. Structure of the ocean–continent transition, location of the continent–ocean boundary and magmatic type of the northern Angolan margin from integrated quantitative analysis of deep seismic reflection and gravity anomaly data. Geol. Soc. London, Spec. Publ. 438, 159–176. https://doi.org/10.1144/SP438.6

Cullen, A., Reemst, P., Henstra, G., Gozzard, S., Ray, A., 2010. Rifting of the South China Sea: new perspectives. Pet. Geosci. 16, 273–282. https://doi.org/10.1144/1354-079309-908

Curray, J.R., 1980. The Ipod Programme on Passive Continental Margins. Philos. Trans. R. Soc. A Math. Phys. Eng. Sci. 294, 17–33. https://doi.org/10.1098/rsta.1980.0008

Davis, J.K., Lavier, L.L., 2017. Influences on the development of volcanic and magma-poor morphologies during passive continental rifting. Geosphere 13, 1524–1540. https://doi.org/10.1130/GES01538.1

de Boer, J., Odom, L.A., Ragland, P.C., Snider, F.G., Tilford, N.R., 1980. The Bataan orogene: Eastward subduction, tectonic rotations, and volcanism in the western Pacific (Philippines). Tectonophysics 67, 251–282. https://doi.org/10.1016/0040-1951(80)90270-X

Dewey, J.F., Bird, J.M., 1970. Mountain belts and the new global tectonics. J. Geophys. Res. 75, 2625–2647. https://doi.org/10.1029/JB075i014p02625

Ding, W., Schnabel, M., Franke, D., Ruan, A., Wu, Z., 2012. Crustal Structure across the Northwestern Margin of South China Sea: Evidence for Magma-poor Rifting from a Wide-angle Seismic Profile. Acta Geol. Sin. - English Ed. 86, 854–866. https://doi.org/10.1111/j.1755-6724.2012.00711.x

Ding, W., Sun, Z., Dadd, K., Fang, Y., Li, J., 2018. Structures within the oceanic crust of the central South China Sea basin and their implications for oceanic accretionary processes. Earth Planet. Sci. Lett. 488, 115–125. https://doi.org/10.1016/j.epsl.2018.02.011

Doo, W. Bin, Hsu, S.K., Armada, L., 2015. New magnetic anomaly map of the east asia with some preliminary tectonic interpretations. Terr. Atmos. Ocean. Sci. 26, 73–81. https://doi.org/10.3319/TAO.2014.08.19.07(GRT)

Duretz, T., Petri, B., Mohn, G., Schmalholz, S.M., Schenker, F.L., Müntener, O., 2016. The importance of structural softening for the evolution and architecture of passive margins. Sci. Rep. 6, 1–7. https://doi.org/10.1038/srep38704

Eagles, G., Pérez-Díaz, L., Scarselli, N., 2015. Getting over continent ocean boundaries. Earth-Science Rev. 151, 244–265. https://doi.org/10.1016/j.earscirev.2015.10.009

Falvey, D.A., 1974. The development of continental margins in plate tectonic theory. APPEA J. 14, 95. https://doi.org/10.1071/AJ73012

Faure, M., Marchadier, Y., Rangin, C., 1989. Pre-Eocene Synmetamorphic Structure in the Mindoro-Romblon-Palawan Area, West Philippines, and implications for the history of southeast Asia. Tectonics 8, 963–979. https://doi.org/10.1029/TC008i005p00963

Fontaine, H., 1979. Note on the geology of the Calamian Islands, North Palawan, Philippines. CCOP Newsletter, Vol. 6, No.2

Fournier, F.T., Borgomano, J., Montaggioni, L.F., 2005. Development patterns and controlling factors of Tertiary carbonate buildups : Insights from high-resolution 3D seismic and well data in the Malampaya gas field (Offshore Palawan, Philippines). Sediment. Geol. 175, 189–215. https://doi.org/10.1016/j.sedgeo.2005.01.009

Franke, D., Barckhausen, U., Baristeas, N., Engels, M., Ladage, S., Lutz, R., Montano, J., Pellejera, N., Ramos, E.G., Schnabel, M., 2011. The continent-ocean transition at the southeastern margin of the South China Sea. Mar. Pet. Geol. 28, 1187–1204. https://doi.org/10.1016/j.marpetgeo.2011.01.004

Franke, D., Savva, D., Pubellier, M., Steuer, S., Mouly, B., Auxietre, J.-L., Meresse, F., Chamot-Rooke, N., 2014. The final rifting evolution in the South China Sea. Mar. Pet. Geol. 58, 704–720. https://doi.org/10.1016/j.marpetgeo.2013.11.020

Gao, J., Wu, S., McIntosh, K., Mi, L., Yao, B., Chen, Z., Jia, L., 2015. The continent-ocean transition at the mid-northern margin of the South China Sea. Tectonophysics 654, 1–19. https://doi.org/10.1016/j.tecto.2015.03.003

Ge, J.W., Zhu, X.M., Zhang, X.T., Jones, B.G., Yu, F.S., Niu, Z.C., Li, M., 2017. Tectono-stratigraphic evolution and hydrocarbon exploration in the Eocene Southern Lufeng Depression, Pearl River Mouth Basin, South China Sea. Aust. J. Earth Sci. 64, 931–956. https://doi.org/10.1080/08120099.2017.1370613

Gee, J.S., Kent, D. V., 2007. Source of Oceanic Magnetic Anomalies and the Geomagnetic Polarity Timescale, in: Treatise on Geophysics. pp. 455–475. https://doi.org/10.1016/B978-044452748-6.00097-3

Gozzard, S., Kusznir, N., Franke, D., Cullen, A., Reemst, P., Henstra, G., 2019. South China Sea crustal thickness and oceanic lithosphere distribution from satellite gravity inversion. Pet. Geosci. 25, 112–128. https://doi.org/10.1144/petgeo2016-162

Haizhang, Y., Ying, C., Mo, J., Yinxue, H., Longying, W., Xuan, H., 2017. Structural evolution differences and the significance for oil and gas exploration in the deep water area of the Pearl River Mouth Basin. China Pet. Explor. 22, 1–11.

Harkin, C., Kusznir, N., Tugend, J., Manatschal, G., McDermott, K., 2019. Evaluating magmatic additions at a magma-poor rifted margin: An East Indian case study. Geophys. J. Int. https://doi.org/10.1093/gji/ggz007

Hayes, D.E., Nissen, S.S., 2005. The South China sea margins: Implications for rifting contrasts. Earth Planet. Sci. Lett. 237, 601–616. https://doi.org/10.1016/j.epsl.2005.06.017

Heezen, B.C., 1960. The Rift in the Ocean Floor. Sci. Am. 203, 98–110. https://doi.org/10.1038/scientificamerican1060-98

Holloway, N., 1981. The North Palawan Block, Philippines: its relation to the Asian Mainland and its role in the evolution of the South China Sea. Bull. Geol. Soc. Malaysia 14, 19–58.

Huismans, R., Beaumont, C., 2011. Depth-dependent extension, two-stage breakup and cratonic underplating at rifted margins. Nature 473, 74–78. https://doi.org/10.1038/nature09988

Jian, Z., Larsen, H.C., Alvarez Zarikian, C.A., Sun, Z., Stock, J.M., Klaus, A., Boaga, J., Bowden, S.A., Briais, A., Chen, Y., Cukur, D., Dadd, K.A., Ding, W., Dorais, M.J., Ferré, E.C., Ferreira, F., Furusawa, A., Gewecke, A.J., Hinojosa, J.L., Höfig, T.W., Hsiung, K.H., Huang, B., Huang, E., Huang, X.L., Jiang, S., Jin, H., Johnson, B.G., Kurzawski, R.M., Lei, C., Li, B., Li, L., Li, Y., Lin, J., Liu, C., Liu, C., Liu, Z., Luna, A., Lupi, C., McCarthy, A.J., Mohn, G., Ningthoujam, L.S., Nirrengarten, M., Osono, N., Peate, D.W., Persaud, P., Qiu, N., Robinson, C.M., Satolli, S., Sauermilch, I., Schindlbeck, J.C., Skinner, S.M., Straub, S.M., Su, X., Tian, L., van der Zwan, F.M., Wan, S., Wu, H., Xiang, R., Yadav, R., Yi, L., Zhang, C., Zhang, J., Zhang, Y., Zhao, N., Zhong, G., Zhong, L., 2018. Site U1505, in: Proceedings of the International Ocean Discovery Program Volume 367/368. https://doi.org/10.14379/iodp.proc.367368.109.2018

Jian, Z., Jin, H., Kaminski, M.A., Ferreira, F., Li, B., Yu, P.-S., 2019. Discovery of the marine Eocene in the northern South China Sea. Natl. Sci. Rev. https://doi.org/10.1093/nsr/nwz084

Karig, D.E., 1983. Accreted terranes in the northern part of the Philippine Archipelago. Tectonics 2, 211–236. https://doi.org/10.1029/TC002i002p00211

Klimetz, M.P., 1983. Speculations on the Mesozoic Plate tectonic evolution of eastern China 2, 139–166. https://doi.org/10.1029/TC002i002p00139

Kudrass, H.R., Wiedicke, M., Cepek, P., Kreuzer, H., Müller, P., 1986. Mesozoic and Cainozoic rocks dredged from the South China Sea (Reed Bank area) and Sulu Sea and their significance for plate-tectonic reconstructions. Mar. Pet. Geol. 3, 19–30. https://doi.org/10.1016/0264-8172(86)90053-X

Kusznir, N.J., Roberts, A.M., Alvey, A.D., 2018. Crustal structure of the conjugate Equatorial Atlantic Margins, derived by gravity anomaly inversion. Geol. Soc. London, Spec. Publ. SP476.5. https://doi.org/10.1144/SP476.5

Larsen, H.C., Jian, Z., Alvarez Zarikian, C.A., Sun, Z., Stock, J.M., Klaus, A., Boaga, J., Bowden, S.A., Briais, A., Chen, Y., Cukur, D., Dadd, K.A., Ding, W., Dorais, M.J., Ferré, E.C., Ferreira, F., Furusawa, A., Gewecke, A.J., Hinojosa, J.L., Höfig, T.W., Hsiung, K.H., Huang, B., Huang, E., Huang, X.L., Jiang, S., Jin, H., Johnson, B.G., Kurzawski, R.M., Lei, C., Li, B., Li, L., Li, Y., Lin, J., Liu, C., Liu, C., Liu, Z., Luna, A., Lupi, C., McCarthy, A.J., Mohn, G., Ningthoujam, L.S., Nirrengarten, M., Osono, N., Peate, D.W., Persaud, P., Qiu, N., Robinson, C.M., Satolli, S., Sauermilch, I., Schindlbeck, J.C., Skinner, S.M., Straub, S.M., Su, X., Tian, L., van der Zwan, F.M., Wan, S., Wu, H., Xiang, R., Yadav, R., Yi, L., Zhang, C., Zhang, J., Zhang, Y., Zhao, N., Zhong, G., Zhong, L., 2018a. Site U1501, in: Proceedings of the International Ocean Discovery Program Volume 367/368. https://doi.org/10.14379/iodp.proc.367368.105.2018

Larsen, H.C., Jian, Z., Alvarez Zarikian, C.A., Sun, Z., Stock, J.M., Klaus, A., Boaga, J., Bowden, S.A., Briais, A., Chen, Y., Cukur, D., Dadd, K.A., Ding, W., Dorais, M.J., Ferré, E.C., Ferreira, F., Furusawa, A., Gewecke, A.J., Hinojosa, J.L., Höfig, T.W., Hsiung, K.H., Huang, B., Huang, E., Huang, X.L., Jiang, S., Jin, H., Johnson, B.G., Kurzawski, R.M., Lei, C., Li, B., Li, L., Li, Y., Lin, J., Liu, C., Liu, C., Liu, Z., Luna, A., Lupi, C., McCarthy, A.J., Mohn, G., Ningthoujam, L.S., Nirrengarten, M., Osono, N., Peate, D.W., Persaud, P., Qiu, N., Robinson, C.M., Satolli, S., Sauermilch, I., Schindlbeck, J.C., Skinner, S.M., Straub, S.M., Su, X., Tian, L., van der Zwan, F.M., Wan, S., Wu, H., Xiang, R., Yadav, R., Yi, L., Zhang, C., Zhang, J., Zhang, Y., Zhao, N., Zhong, G., Zhong, L., 2018b. Site U1502, in: Proceedings of the International Ocean Discovery Program Volume

367/368. https://doi.org/10.14379/iodp.proc.367368.106.2018

Larsen, H.C., Jian, Z., Alvarez Zarikian, C.A., Sun, Z., Stock, J.M., Klaus, A., Boaga, J., Bowden, S.A., Briais, A., Chen, Y., Cukur, D., Dadd, K.A., Ding, W., Dorais, M.J., Ferré, E.C., Ferreira, F., Furusawa, A., Gewecke, A.J., Hinojosa, J.L., Höfig, T.W., Hsiung, K.H., Huang, B., Huang, E., Huang, X.L., Jiang, S., Jin, H., Johnson, B.G., Kurzawski, R.M., Lei, C., Li, B., Li, L., Li, Y., Lin, J., Liu, C., Liu, C., Liu, Z., Luna, A., Lupi, C., McCarthy, A.J., Mohn, G., Ningthoujam, L.S., Nirrengarten, M., Osono, N., Peate, D.W., Persaud, P., Qiu, N., Robinson, C.M., Satolli, S., Sauermilch, I., Schindlbeck, J.C., Skinner, S.M., Straub, S.M., Su, X., Tian, L., van der Zwan, F.M., Wan, S., Wu, H., Xiang, R., Yadav, R., Yi, L., Zhang, C., Zhang, J., Zhang, Y., Zhao, N., Zhong, G., Zhong, L., 2018c. Site U1504, in: Proceedings of the International Ocean Discovery Program Volume 367/368. https://doi.org/10.14379/iodp.proc.367368.108.2018

Larsen, H.C., Mohn, G., Nirrengarten, M., Sun, Z., Stock, J., Jian, Z., Klaus, A., Alvarez-Zarikian, C.A., Boaga, J., Bowden, S.A., Briais, A., Chen, Y., Cukur, D., Dadd, K., Ding, W., Dorais, M., Ferré, E.C., Ferreira, F., Furusawa, A., Gewecke, A., Hinojosa, J., Höfig, T.W., Hsiung, K.H., Huang, B., Huang, E., Huang, X.L., Jiang, S., Jin, H., Johnson, B.G., Kurzawski, R.M., Lei, C., Li, B., Li, L., Li, Y., Lin, J., Liu, C., Liu, C., Liu, Z., Luna, A.J., Lupi, C., McCarthy, A., Ningthoujam, L., Osono, N., Peate, D.W., Persaud, P., Qiu, N., Robinson, C., Satolli, S., Sauermilch, I., Schindlbeck, J.C., Skinner, S., Straub, S., Su, X., Su, C., Tian, L., van der Zwan, F.M., Wan, S., Wu, H., Xiang, R., Yadav, R., Yi, L., Yu, P.S., Zhang, C., Zhang, J., Zhang, Y., Zhao, N., Zhong, G., Zhong, L., 2018d. Rapid transition from continental breakup to igneous oceanic crust in the South China Sea. Nat. Geosci. 11, 782–789. https://doi.org/10.1038/s41561-018-0198-1

Larsen, H.C., Sun, Z., Stock, J.M., Jian, Z., Alvarez Zarikian, C.A., Klaus, A., Boaga, J., Bowden, S.A., Briais, A., Chen, Y., Cukur, D., Dadd, K.A., Ding, W., Dorais, M.J., Ferré, E.C., Ferreira, F., Furusawa, A., Gewecke, A.J., Hinojosa, J.L., Höfig, T.W., Hsiung, K.H., Huang, B., Huang, E., Huang, X.L., Jiang, S., Jin, H., Johnson, B.G., Kurzawski, R.M., Lei, C., Li, B., Li, L., Li, Y., Lin, J., Liu, C., Liu, C., Liu, Z., Luna, A., Lupi, C., McCarthy, A.J., Mohn, G., Ningthoujam, L.S., Nirrengarten, M., Osono, N., Peate, D.W., Persaud, P., Qiu, N., Robinson, C.M., Satolli, S., Sauermilch, I., Schindlbeck, J.C., Skinner, S.M., Straub, S.M., Su, X., Tian, L., van der Zwan, F.M., Wan, S., Wu, H., Xiang, R., Yadav, R., Yi, L., Zhang, C., Zhang, J., Zhang, Y., Zhao, N., Zhong, G., Zhong, L., 2018e. Expedition 367/368 summary, in: Proceedings of the International Ocean Discovery Program Volume 367/368. https://doi.org/10.14379/iodp.proc.367368.101.2018

Le Pourhiet, L., Chamot-Rooke, N., Delescluse, M., May, D.A., Watremez, L., Pubellier, M., 2018. Continental break-up of the South China Sea stalled by far-field compression. Nat. Geosci. https://doi.org/10.1038/s41561-018-0178-5

Lei, C., Alves, T.M., Ren, J., Pang, X., Yang, L., Liu, J., 2019. Depositional architecture and structural evolution of a region immediately inboard of the locus of continental. Geol. Soc. Am. 1–16. https://doi.org/10.1130/B35001.1/4637903/b35001.pdf

Lei, C., Ren, J., 2016. Hyper-extended rift systems in the Xisha Trough, northwestern South China Sea: Implications for extreme crustal thinning ahead of a propagating ocean. Mar. Pet. Geol. 77, 846–864. https://doi.org/10.1016/j.marpetgeo.2016.07.022

Lei, C., Ren, J., Pang, X., Chao, P. and Han, X., 2018. Continental rifting and sediment infill in the distal part of the northern South China Sea in the Western Pacific region: Challenge on the present-day models for the passive margins. Marine and Petroleum Geology, 93: 166-181.

Lester, R., Van Avendonk, H.J.A., McIntosh, K., Lavier, L., Liu, C.S., Wang, T.K., Wu, F., 2014. Rifting and magmatism in the northeastern South China Sea from wide-angle tomography and seismic reflection imaging. J. Geophys. Res. Solid Earth 119, 2305–2323. https://doi.org/10.1002/2013JB010639

Li, C.-F., Lin, J., Kulhanek, D.K., Williams, T., Bao, R., Briais, A., Brown, E.A., Chen, Y., Clift, P.D., Colwell, F.S., Dadd, K.A., Ding, W.-W., Hernández-Almeida, I., Huang, X.-L., Hyun, S., Jiang, T., Koppers, A.A.P., Li, Q., Liu, C., Liu, Q., Liu, Z., Nagai, R.H., Peleo-Alampay, A., Su, X., Sun, Z., Tejada, M.L.G., Trinh, H.S., Yeh, Y.-C., Zhang, C., Zhang, F., Zhang, G.-L., Zhao, X., 2015. Expedition 349 summary, in: Proceedings of the International Ocean Discovery Program Volume 349. https://doi.org/10.14379/iodp.proc.349.101.2015

Li, C.-F., Xu, X., Lin, J., Sun, Z., Zhu, J., Yao, Y., Zhao, X., Liu, Q., Kulhanek, D.K., Wang, J., Song, T., Zhao, J., Qiu, N., Guan, Y., Zhou, Z., Williams, T., Bao, R., Briais, A., Brown, E.A., Chen, Y., Clift, P.D., Colwell, F.S., Dadd, K.A., Ding, W., Almeida, I.H., Huang, X.-L., Hyun, S., Jiang, T., Koppers, A.A.P., Li, Q., Liu, C., Liu, Z., Nagai, R.H., Peleo-Alampay, A., Su, X., Tejada, M.L.G., Trinh, H.S., Yeh, Y.-C., Zhang, C., Zhang, F., Zhang, G.-L., 2014. Ages and magnetic structures of the South China Sea constrained by deep tow magnetic surveys and IODP Expedition 349. Geochemistry, Geophys. Geosystems 15, 4958–4983. https://doi.org/10.1002/2014GC005567

Li, C., Zhou, Z., Hao, H., Chen, B., Chen, H., Wang, J., Wu, J., 2008. Late Mesozoic tectonic structure and evolution along the present-day northeastern South China Sea continental margin. J. Asian Earth Sci. 31, 546–561. https://doi.org/10.1016/j.jseaes.2007.09.004

Li, J., Zhang, Y., Dong, S., Johnston, S.T., 2014. Cretaceous tectonic evolution of South China: A preliminary synthesis. Earth-Science Rev. 134, 98–136. https://doi.org/10.1016/j.earscirev.2014.03.008

Li, Z., Li, X.-H., 2007. Formation of the 1300-km-wide intracontinental orogen and postorogenic magmatic province in Mesozoic South China : A flat-slab subduction model. Geology 35, 179–182. https://doi.org/10.1130/G23193A.1

Ligi, M., Bonatti, E., Bosworth, W., Cai, Y., Cipriani, A., Palmiotto, C., Ronca, S., Seyler, M., 2018. Birth of an ocean in the Red Sea: Oceanic-type basaltic melt intrusions precede continental rupture. Gondwana Res. 54, 150–160. https://doi.org/10.1016/j.gr.2017.11.002

Ludwig, W.J., Nafe, J.E., Drake, C.L., 1970. Seismic refraction., in: Maxwell, A.E. (Ed.), The Sea. New-York, pp. 53–84.

McKenzie, D., 1978. Some remarks on the formation of sedimentary basins. Earth Planet. Sci. Lett. 40, 25–32.

Mckenzie, D., Bickle, M.J., 1988. The volume and composition of melt generated by extension of the lithosphere. J. Petrol. 29, 1–55.

Meyer, B., Saltus, R., Chulliat, A., 2017. EMAG2: Earth Magnetic Anomaly Grid (2-arc-minute resolution) Version 3. https://doi.org/10.7289/V5H70CVX

Mohn, G., Karner, G.D., Manatschal, G., Johnson, C.A., 2015. Structural and stratigraphic evolution of the Iberia-Newfoundland hyper-extended rifted margin: a quantitative modelling approach. Geol. Soc. London, Spec. Publ. 15, 13810. https://doi.org/10.1144/SP413.9

Morley, C.K., 2016. Major unconformities/termination of extension events and associated surfaces in the South China Seas: Review and implications for tectonic development. J. Asian Earth Sci. 120, 62–86. https://doi.org/10.1016/j.jseaes.2016.01.013

Müller, R.D., Sdrolias, M., Gaina, C., Roest, W.R., 2008. Age, spreading rates, and spreading asymmetry of the world's ocean crust. Geochemistry, Geophys. Geosystems 9, 1–19. https://doi.org/10.1029/2007GC001743

Müller, R.D., Seton, M., Zahirovic, S., Williams, S.E., Matthews, K.J., Wright, N.M., Shephard, G.E., Maloney, K.T., Barnett-Moore, N., Hosseinpour, M., Bower, D.J., Cannon, J., 2016. Ocean Basin Evolution and Global-Scale Plate Reorganization Events Since Pangea Breakup. Annu. Rev. Earth Planet. Sci. 44, 107–138. https://doi.org/10.1146/annurev-earth-060115-012211

Nagel, T.J., Buck, W.R., 2007. Control of rheological stratification on rifting geometry: A symmetric model resolving the upper plate paradox. Int. J. Earth Sci. 96, 1047–1057. https://doi.org/10.1007/s00531-007-0195-x

Nanni, U., Pubellier, M., Chan, L.S., Sewell, R.J., 2017. Rifting and reactivation of a Cretaceous structural belt at the northern margin of the South China Sea. J. Asian Earth Sci. 136, 110–123. https://doi.org/10.1016/j.jseaes.2017.01.008

Nirrengarten, M., Manatschal, G., Tugend, J., Kusznir, N., Sauter, D., 2018. Kinematic evolution of the Southern North Atlantic: Implications for the formation of hyperextended rift systems. Tectonics 37, 89–118. https://doi.org/10.1002/2017TC004495

Parker, R.L., 1972. The rapid calculation of potential anomalies, Geophys J. R. astr. Soc., 31, 447–455

Pérez-Gussinyé, M., Ranero, C.R., Reston, T.J., Sawyer, D., 2003. Mechanisms of extension at nonvolcanic margins: Evidence from the Galicia interior basin, west of Iberia. J. Geophys. Res. Solid Earth 108, 1–19. https://doi.org/10.1029/2001JB000901

Peron-Pinvidic, G., Manatschal, G., Osmundsen, P.T., 2013. Structural comparison of archetypal Atlantic rifted margins: A review of observations and concepts. Mar. Pet. Geol. 43, 21–47. https://doi.org/10.1016/j.marpetgeo.2013.02.002

Petri, B., Duretz, T., Mohn, G., Schmalholz, S.M., Karner, G.D., Müntener, O., 2019. Thinning mechanisms of heterogeneous continental lithosphere. Earth Planet. Sci. Lett. 512, 147–162. https://doi.org/10.1016/j.epsl.2019.02.007

Pichot, T., Delescluse, M., Chamot-Rooke, N., Pubellier, M., Qiu, Y., Meresse, F., Sun, G., Savva, D., Wong, K.P., Watremez, L., Auxiètre, J.L., 2014. Deep crustal structure of the conjugate margins of the SW South China Sea from wide-angle refraction seismic data. Mar. Pet. Geol. 58, 627–643. https://doi.org/10.1016/j.marpetgeo.2013.10.008

Pin, Y., Di, Z., Zhaoshu, L., 2001. A crustal structure pro file across the northern continental margin of the South China Sea. Tectonophysics 338.

Pubellier, M., Ali, J., Monnier, C., 2003. Cenozoic Plate interaction of the Australia and Philippine Sea Plates: “hit-and-run” tectonics. Tectonophysics 363, 181–199. https://doi.org/10.1016/S0040-1951(02)00671-6

Pubellier, M., Meresse, F., 2013. Phanerozoic growth of Asia: Geodynamic processes and evolution. J. Asian Earth Sci. 72, 118–128. https://doi.org/10.1016/j.jseaes.2012.06.013

Pubellier, M., D. Savva, M. Aurelio, F. Sapin, 2017 Structural Map of the South China Sea, CCGM-CGMW doi:10.14682/2017STRUCTUSCS

Reston, T.J., 2009. The structure, evolution and symmetry of the magma-poor rifted margins of the North and Central Atlantic: A synthesis. Tectonophysics 468, 6–27. https://doi.org/10.1016/j.tecto.2008.09.002

Ru, K., Pigott, J.D., 1986. Episodic rifting and subsidence in the South China Sea. Am. Assoc. Pet. Geol. Bull. 70, 1136–1155. https://doi.org/10.1306/94886A8D-1704-11D7-8645000102C1865D

Sandwell, D.T., Müller, R.D., Smith, W.H.F., Garcia, E., Francis, R., 2014. New global marine gravity model from CryoSat-2 and Jason-1 reveals buried tectonic structure. Science (80-.). 346, 65–67. https://doi.org/10.1126/science.1258213

Savva, D., Pubellier, M., Franke, D., Chamot-Rooke, N., Meresse, F., Steuer, S., Auxietre, J.L., 2014. Different expressions of rifting on the South China Sea margins. Mar. Pet. Geol. 58, 579–598. https://doi.org/10.1016/j.marpetgeo.2014.05.023

Schlüter, H.U., Hinz, K., Block, M., 1996. Tectono-stratigraphic terranes and detachment faulting of the South China Sea and Sulu Sea. Mar. Geol. 130, 39–78. https://doi.org/10.1016/0025-3227(95)00137-9

Sclater, J.G., Jaupart, C., Galson, D., 1980. The heat flow through oceanic and continental crust and the heat loss of the Earth. Rev. Geophys. 18, 269–311. https://doi.org/10.1029/RG018i001p00269

Seton, M., Whittaker, J.M., Wessel, P., Müller, R.D., DeMets, C., Merkouriev, S., Cande, S., Gaina, C., Eagles, G., Granot, R., Stock, J., Wright, N., Williams, S.E., 2014. Community infrastructure and repository for marine magnetic identifications. Geochemistry, Geophys. Geosystems 15, 1629–1641. https://doi.org/10.1002/2013GC005176

Sibuet, J.C., Yeh, Y.C., Lee, C.S., 2016. Geodynamics of the South China Sea. Tectonophysics 692, 98–119. https://doi.org/10.1016/j.tecto.2016.02.022

Sizhong, P., Cunmin, C., 1993. Geology and geochemistry of source rocks of the Eastern Pearl River Mouth Basin, South China Sea. J. Southeast Asian Earth Sci. 8, 393–406. https://doi.org/10.1016/0743-9547(93)90041-M

Smith, R.A., 1961. A uniqueness theorem concerning gravity fields, Proc. Cambridge Philos. Soc., 57, 865–70

Stein, S., Melosh, H.J., Minster, J.B., 1977. Ridge migration and asymmetric sea-floor spreading. Earth Planet. Sci. Lett. 36, 51–62. https://doi.org/10.1016/0012-821X(77)90187-X

Steuer, S., Franke, D., Meresse, F., Savva, D., Pubellier, M., Auxietre, J.L., Aurelio, M., 2013. Time constraints on the evolution of southern Palawan Island, Philippines from onshore and offshore correlation of Miocene limestones. J. Asian Earth Sci. 76, 412–427. https://doi.org/10.1016/j.jseaes.2013.01.007

Stock, J.M., Sun, Z., Klaus, A., Larsen, H.C., Jian, Z., Alvarez Zarikian, C.A., Boaga, J., Bowden, S.A., Briais, A., Chen, Y., Cukur, D., Dadd, K.A., Ding, W., Dorais, M.J., Ferré, E.C., Ferreira, F., Furusawa, A., Gewecke, A.J., Hinojosa, J.L., Höfig, T.W., Hsiung, K.H., Huang, B., Huang, E., Huang, X.L., Jiang, S., Jin, H., Johnson, B.G., Kurzawski, R.M., Lei, C., Li, B., Li, L., Li, Y., Lin, J., Liu, C., Liu, C., Liu, Z., Luna, A., Lupi, C., McCarthy, A.J., Mohn, G., Ningthoujam, L.S., Nirrengarten, M., Osono, N., Peate, D.W., Persaud, P., Qiu, N., Robinson, C.M., Satolli, S., Sauermilch, I., Schindlbeck, J.C., Skinner, S.M., Straub, S.M., Su, X., Tian, L., van der Zwan, F.M., Wan, S., Wu, H., Xiang, R., Yadav, R., Yi, L., Zhang, C., Zhang, J., Zhang, Y., Zhao, N., Zhong, G., Zhong, L., 2018. Site U1500, in: Proceedings of the International Ocean Discovery Program Volume 367/368. https://doi.org/10.14379/iodp.proc.367368.104.2018

Sun, Z., Stock, J.M., Klaus, A., Larsen, H.C., Jian, Z., Alvarez Zarikian, C.A., Boaga, J., Bowden, S.A., Briais, A., Chen, Y., Cukur, D., Dadd, K.A., Ding, W., Dorais, M.J., Ferré, E.C., Ferreira, F., Furusawa, A., Gewecke, A.J., Hinojosa, J.L., Höfig, T.W., Hsiung, K.H., Huang, B., Huang, E., Huang, X.L., Jiang, S., Jin, H., Johnson, B.G., Kurzawski, R.M., Lei, C., Li, B., Li, L., Li, Y., Lin, J., Liu, C., Liu, C., Liu, Z., Luna, A., Lupi, C., McCarthy, A.J., Mohn, G., Ningthoujam, L.S., Nirrengarten, M., Osono, N., Peate, D.W., Persaud, P., Qiu, N., Robinson, C.M., Satolli, S., Sauermilch, I., Schindlbeck, J.C., Skinner, S.M., Straub, S.M., Su, X., Tian, L., van der Zwan, F.M., Wan, S., Wu, H., Xiang, R., Yadav, R., Yi, L., Zhang, C., Zhang, J., Zhang, Y., Zhao, N., Zhong, G., Zhong, L., 2018. Site U1499, in: Proceedings of the International Ocean Discovery Program Volume 367/368. https://doi.org/10.14379/iodp.proc.367368.103.2018

Taylor, B., Goodliffe, A.M., Martinez, F., 1999. How continents break up: Insights from Papua New Guinea. J. Geophys. Res. 104, 7497. https://doi.org/10.1029/1998JB900115

Taylor, B., Hayes, D., 1983. Origin and history of the South China Sea basin, in: Hayes, D. (Ed.), The Tectonic and Geologic Evolution of Southeast Asian Seas and Islands: Part 2. pp. 23–56.

Tugend, J., Manatschal, G., Kusznir, N.J., Masini, E., 2015. Characterizing and identifying structural domains at rifted continental margins: application to the Bay of Biscay margins and its Western Pyrenean fossil remnants. Geol. Soc. London, Spec. Publ. 413, 171–203. https://doi.org/10.1144/SP413.3

Tucholke, B.E., Sawyer, D.S., Sibuet, J.-C., 2007. Breakup of the Newfoundland–Iberia rift. Geol. Soc. London, Spec. Publ. 282, 9–46. https://doi.org/10.1144/SP282.2

Tucholke, B.E., Sibuet, J.-C., 2007. Leg 210 Synthesis: Tectonic, Magmatic, and Sedimentary Evolution of the Newfoundland-Iberia Rift, in: Proceedings of the Ocean Drilling Program, 210 Scientific Results. https://doi.org/10.2973/odp.proc.sr.210.101.2007

Wang, J., Pang, X., Liu, B., Zheng, J., Wang, H., 2018. The Baiyun and Liwan Sags: Two supradetachment basins on the passive continental margin of the northern South China Sea. Mar. Pet. Geol. 95, 206–218. https://doi.org/10.1016/j.marpetgeo.2018.05.001

Wang, P., Prell, W.L., Blum, P., 2000. Leg 184 Summary: Exploring the Asian Monsoon through Drilling in the South China Sea, in: Proceedings of the Ocean Drilling Program, 184 Initial Reports, Proceedings of the Ocean Drilling Program. Ocean Drilling Program. https://doi.org/10.2973/odp.proc.ir.184.101.2000

Wang, T.K., Chen, M.K., Lee, C.S., Xia, K., 2006. Seismic imaging of the transitional crust across the northeastern margin of the South China Sea. Tectonophysics 412, 237–254. https://doi.org/10.1016/j.tecto.2005.10.039

Whitmarsh, R.B., Manatschal, G., Minshull, T.A., 2001. Evolution of magma-poor continental margins from rifting to seafloor spreading. Nature 413, 150–154. https://doi.org/10.1038/35093085

Whitmarsh, R.B., Sawyer, D.S., Klaus, A., Masson, D.G. (Eds.), 1996. Proceedings of the Ocean Drilling Program, 149 Scientific Results, Proceedings of the Ocean Drilling Program. Ocean Drilling Program. https://doi.org/10.2973/odp.proc.sr.149.1996

Whitmarsh, R.B., Wallace, P.J., 2001. Proceedings of the Ocean Drilling Program, 173 Scientific Results 173. https://doi.org/10.2973/odp.proc.sr.173.2001

Whittaker, J.M., Goncharov, A., Williams, S.E., Müller, R.D., Leitchenkov, G., 2013. Global sediment thickness data set updated for the Australian-Antarctic Southern Ocean. Geochemistry, Geophys. Geosystems 14, 3297–3305. https://doi.org/10.1002/ggge.20181

Williams, H.H., 1997. Play concepts-northwest Palawan, Philippines. J. Asian Earth Sci. 15, 251–273. https://doi.org/10.1016/S0743-9547(97)00011-1

Xia, S., Liu, Z., Luo, D., Shu, L., Zhang, Z., Gao, L., Dong, G., Zhang, L., Leng, C., Zhang, B., 2018. Sequence architecture and depositional evolution in Lufeng Depression, Pearl River Mouth Basin, South China Sea Part A: The braided delta deposits of Cenozoic Enping Formation. Geol. J. https://doi.org/10.1002/gj.3117

Yang, L., Ren, J., McIntosh, K., Pang, X., Chao, L., Zhao, Y., 2018. The structure and evolution of deepwater basins in the distal margin of the northern South China Sea and their implications for the formation of the continental margin. Mar. Pet. Geol. 92, 234–254. https://doi.org/10.1016/j.marpetgeo.2018.02.032

Ye, Q., Mei, L., Shi, H., Shu, Y., Camanni, G., Wu, J., 2018. A low-angle normal fault and basement structures within the Enping Sag, Pearl River Mouth Basin: Insights into late Mesozoic to early Cenozoic tectonic evolution of the South China Sea area. Tectonophysics 731–732, 1–16. https://doi.org/10.1016/j.tecto.2018.03.003

Zahirovic, S., Seton, M., Müller, R.D., 2014. The Cretaceous and Cenozoic tectonic evolution of Southeast Asia. Solid Earth 5, 227–273. https://doi.org/10.5194/se-5-227-2014

Zhang, C., Su, M., Pang, X., Zheng, J., Liu, B., Sun, Z., Manatschal, G., 2019. Tectono-Sedimentary Analysis of the Hyperextended Liwan Sag Basin (Midnorthern Margin of the South China Sea). Tectonics. https://doi.org/10.1029/2018TC005063

Zhao, M., Qiu, X., Xia, S., Xu, H., Wang, P., Wang, T.K., Lee, C.S., Xia, K., 2010. Seismic structure in the northeastern South China Sea: S-wave velocity and Vp/Vs ratios derived from three-component OBS data. Tectonophysics 480, 183–197. https://doi.org/10.1016/j.tecto.2009.10.004

Zhou, D., Ru, K., Chen, H., 1995. Kinematics of Cenozoic extension on the South China Sea continental margin and its implications for the tectonic evolution of the region. Tectonophysics 251, 161–177. https://doi.org/10.1016/0040-1951(95)00018-6

Zhou, Z., Mei, L., Liu, J., Zheng, J., Chen, L., Hao, S., 2018. Continentward-dipping detachment fault system and asymmetric rift structure of the Baiyun Sag, northern South China Sea. Tectonophysics 726, 121–136. https://doi.org/10.1016/j.tecto.2018.02.002